Lawrence Berkeley Laboratory
UNIVERSITY OF CALIFORNIA

Physics Division

A New Limit on the Neutrinoless Double Beta Decay of ^{100}Mo

J.M. Krivicich
(Ph.D. Thesis)

March 1988

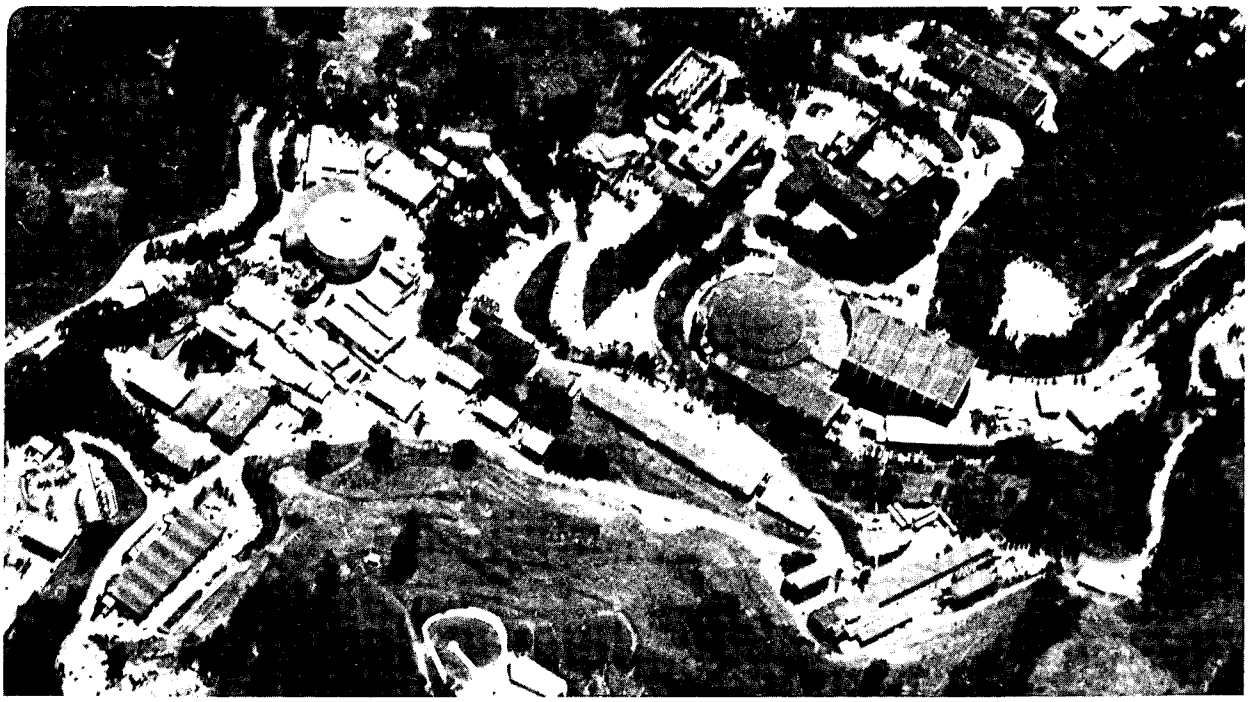

Prepared for the U.S. Department of Energy under Contract Number DE-AC03-76SF00098.

DISCLAIMER

LBL-25233

A New Limit on the Neutrinoless Double Beta Decay of ^{100}Mo

Joseph Mario Krivicich

Ph.D. Thesis

March 1988

Lawrence Berkeley Laboratory

University of California

Berkeley, CA 94720

This work was supported by the Director, Office of Energy Research, Office of High Energy and Nuclear Physics, Division of High Energy Physics of the U. S. Department of Energy under contract #DE-AC03-76SF00098.

A New Limit on the Neutrinoless Double Beta Decay of ^{100}Mo

By

Joseph Mario Krivicich

March 23, 1988

Abstract

A search for the neutrinoless double beta decay of ^{100}Mo was conducted using thin Mo films and solid state Si detectors. The experiment has collected 3500 hours of data operating underground in a deep silver mine (3290 M.W.E). Only one event was found to be consistent with neutrinoless double beta decay. Using this one event, a limit of $\geq 1 \times 10^{22}$ years (1σ) is set on the ^{100}Mo half-life. This is approximately five times larger than the best previous ^{100}Mo limit.

Contents

Acknowledgements

The experiment described in this thesis is the result of the efforts of many people. First, I would like to thank Dr. Robert Kenney and Professor A. C. Helmholz for acting as my advisors over the past seven years and as co-chairman of my thesis committee. Both have contributed greatly to my education as a physicist. In particular, I would like to mention their constant encouragement of my efforts during the writing of this thesis, which at the time may not have been appreciated as much as it is now.

In addition, I would like to thank the other physicists who worked on this project, especially: Margaret Alston-Garnjost and Brian Dougherty of the Lawrence Berkeley Laboratory; and Howard Nicholson of Mt. Holyoke College. Their comments and conversations on various topics over the years proved to be invaluable.

I would also like to thank Mike Long and Sue Daly who built much of the apparatus used in this experiment during its long evolution from a two-detector array in building 50A at LBL to the current version 4000 ft. underground. Their midafternoon conversations on non-scientific matters also helped me to keep my sanity and were much appreciated.

Finally, I would like to thank Vernon Benz and Jim Van Kuiken for keeping me awake on those early morning trips down into the mine.

This work was done under the auspices of the U.S. Department of Energy (Contracts DE-AC03-76FO00098, DE-AC02-78ER04831 and DE-AS04-76ER03347).

Chapter 1

Introduction

In an attempt to look for physics beyond the standard model, non-accelerator experiments have become increasingly important. Experiments on tritium beta decay have put limits on the mass of the neutrino by looking at the shape of the beta decay spectrum near its endpoint. Underground experiments look for proton decay and have measured the flux of electron neutrinos from the sun. The solar neutrino experiment of Davis detects a lower flux than predicted by the standard solar model [1]. This may be evidence for matter enhanced neutrino oscillations (MSW effect) [2]. Proton decay has not been detected, but these experiments have made the first observation of neutrinos from a supernova(1987a), a spectacular result [3].

The experiment described in this thesis looks for the double beta decay of ^{100}Mo. Double beta decay is a second order weak interaction process. The standard

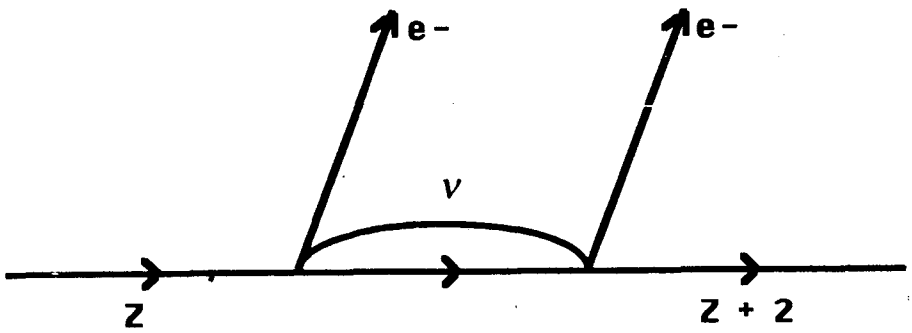

Figure 1.1: **Neutrinoless double beta decay**

model allows the two neutrino decay,

$$N^Z \Longrightarrow N^{Z+2} + 2e^- + 2\bar{\nu} \tag{1.1}$$

but forbids the neutrinoless decay.

$$N^Z \Longrightarrow N^{Z+2} + 2e^- \tag{1.2}$$

Since reaction (1.2) violates lepton number conservation, special conditions must be met for this decay to occur. The neutrinoless mode is mediated by a virtual neutrino (figure 1.1). An antineutrino emitted along with the electron at the first vertex cannot be absorbed as a neutrino at the second vertex. The neutrino must be its own antiparticle, a Majorana neutrino. In addition, helicity is absolutely conserved for a massless particle and the $V - A$ structure of the weak interaction requires the emitted neutrino to be left handed and the absorbed neutrino to be right handed. The neutrino must be massive to break helicity conservation or there must be a $V + A$ contribution to the weak interaction to allow the absorption of a right-handed particle.

These conditions represent new physics beyond the standard model. In grand unified theories (GUTS), the electro-weak and strong force are joined into a single fundamental interaction, blurring the distinction between quarks and leptons. Baryon and lepton number are no longer conserved. Since neutrinos and all other leptons are in the same multiplet as the quarks, neutrinos are expected to be massive. Left-right symmetric theories postulate the return of parity conservation at some high energy. This necessitates the introduction of a $V + A$ interaction. In gauge theories only the fundamental gauge symmetry must be exact. The $U(1)$ symmetry of electrodynamics (i.e. charge conservation) forces charged fermions to be Dirac particles. A Dirac particle can be viewed as a linear combination of two mass degenerate Majorana particles. Since the neutrino is electrically neutral, there is no conservation law to force the mass degeneracy and neutrinos are expected to be Majorana particles.

Neutrinoless double beta decay has long been recognized as a sensitive test of lepton number conservation and of the properties of the electron neutrino. Expectations arising from GUTS mentioned above, have renewed experimental interest in this process in recent years. Double beta decay has been detected by geochemical measurements on a number of isotopes [4][5]; however this technique cannot distinguish between decay modes. The two neutrino decay of ^{82}Se has been detected recently in the laboratory. A half-life of 1×10^{20} years was measured [6]. The neutrinoless reaction (1.2) has not been observed by experiments of any type.

Chapter 2

General Background

2.1 Energetics and Spin-Parity

To observe double beta decay in a particular isotope, it is necessary that ordinary beta decay be energetically forbidden or highly suppressed. This happens in even-even nuclei, because the pairing force acting between like nucleons increases the binding energy of these nuclei relative to their odd-odd neighbors (figure 2.1). Double beta decay may then be allowed, if for a given atomic mass number A, the nucleus of charge $Z+2$ is at a lower mass than the nuclei of charge Z. If the opposite is true double positron decay can occur, but the rate for this process is suppressed relative to double beta decay because of the coulomb repulsion between nucleus and positron. Double K capture can also occur. The rate is estimated to be between that of double beta decay and double positron decay [7]. Experimentally, this decay is very difficult to observe because the final state nucleus is accompanied by only the two neutrinos. The neutrinoless process is a resonance

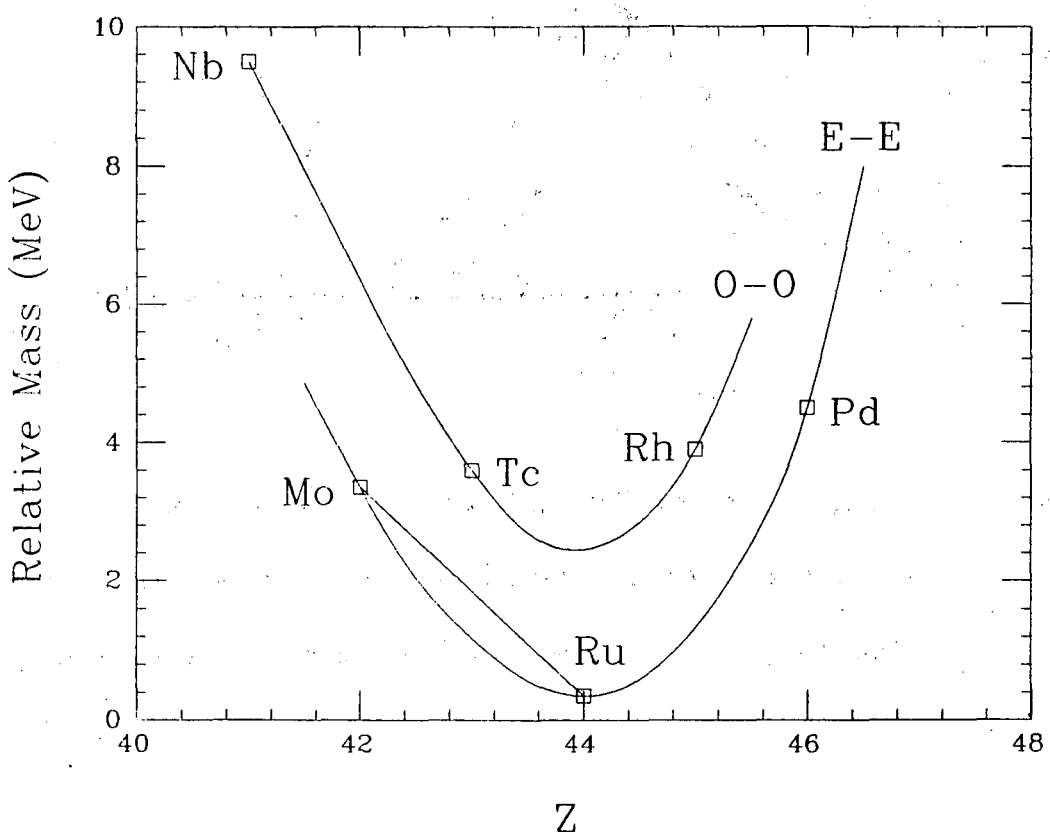

Figure 2.1: **Mass 100 isobars.** The ^{100}Mo to ^{100}Tc beta decay is energetically forbidden. The double beta decay to ^{100}Ru is allowed.

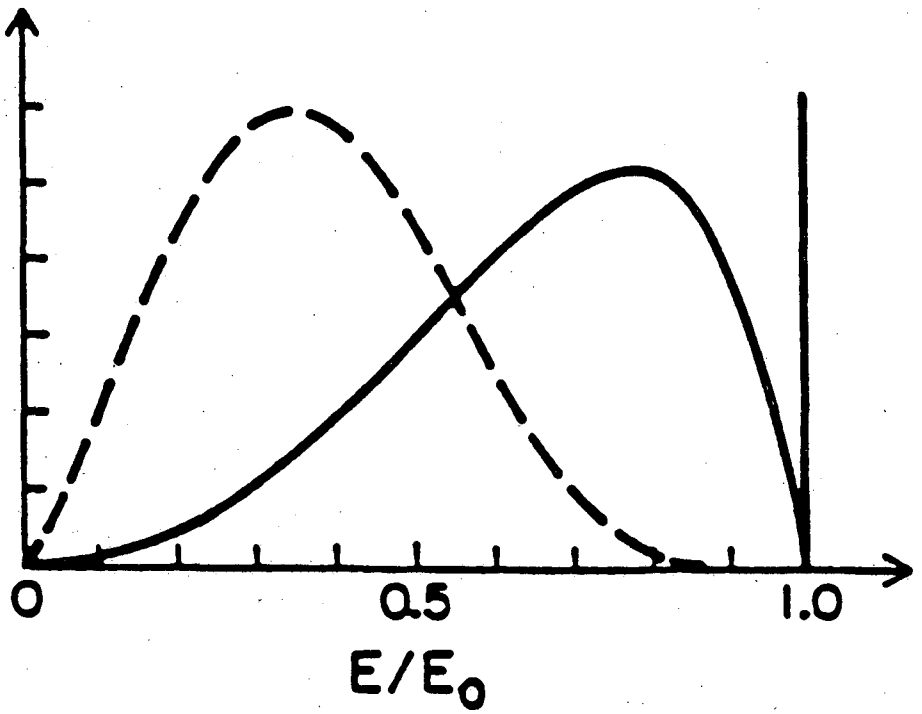

Figure 2.2: **Sum energy spectrum.** The dashed line is the two neutrino spectrum. The spike at the total decay energy is from the neutrinoless decay. The solid line is the majoron decay spectrum (see section 2.4) The relative normalization is arbitrary.

reaction and cannot occur unless there is an accidental matching of initial and final state energies. In all cases, intial and final states are even-even nuclei, with the pairing force leading to spin 0 parity even ($J^P = 0^+$) ground states. Low lying excited states of daughter nuclei are $J^P = 1^+$ or $J^P = 2^+$, so only $0^+ \rightarrow J^+$ transitions ($J = 0, 1, 2$) need be considered [8].

Experimentally, two neutrino double beta decay can be distinguished from the neutrinoless mode by looking at the electron sum energy spectrum (figure 2.2). In

the two neutrino mode the energy is shared between the electrons and neutrinos. Since the neutrinos are not detected, a broad beta-decay-like spectrum results. For the neutrinoless mode all the energy is carried by the two electrons and a peak occurs at the decay energy E, the width of the measured peak being determined by the resolution of the detection system. In both cases the recoil of the final state nucleus takes very little energy away from the other particles. This is estimated in ^{100}Mo to be at most, $E^2/2M = 45$ eV where $E = 3$ MeV and $M = 100$ GeV.

2.2 Majorana Neutrinos

Majorana neutrinos are their own antiparticles. To see how this situation arises, consider a spinor field with a standard (Dirac) mass term in its Lagrangian.

$$m_d\bar{\psi}\psi \tag{2.1}$$

Since $\bar{\psi}\psi = \bar{\psi}_c\psi_c$, where $\psi_c = i\gamma_2\psi^\dagger$ is the charge conjugate field. The mass term can be written as.

$$m_d(\bar{\psi}\psi + \bar{\psi}_c\psi_c)/2 \tag{2.2}$$

Now suppose additional mass terms $\frac{1}{2}M\bar{\psi}\psi_c$ and $\frac{1}{2}M'\bar{\psi}_c\psi$ are added. These are Majorana Mass term. If CP conservation is assumed for the weak interaction, M is real and $M = M'$. The mass term becomes,

$$m_d(\bar{\psi}\psi + \bar{\psi}_c\psi_c)/2 + M(\bar{\psi}_c\psi + \bar{\psi}\psi_c)/2 = \frac{1}{2}\begin{pmatrix} \bar{\psi} & \bar{\psi}_c \end{pmatrix}\begin{pmatrix} m_d & M \\ M & m_d \end{pmatrix}\begin{pmatrix} \psi \\ \psi_c \end{pmatrix} \tag{2.3}$$

where matrix notation is used on the right side of the equation [9]. The mass matrix can be diagonalized by a unitary transformation, using the matrix.

$$U = \frac{1}{\sqrt{2}} \begin{pmatrix} 1 & 1 \\ 1 & -1 \end{pmatrix} \tag{2.4}$$

The mass matrix and mass eigenstates N are then.

$$\begin{pmatrix} m_d + M & 0 \\ 0 & m_d - M \end{pmatrix} \quad N_{\pm} = \frac{1}{\sqrt{2}}(\psi \pm \psi_c) \tag{2.5}$$

These are Majorana fields. They are invariant under charge conjugation.

If the Majorana mass term M were identically zero, it would seem that any linear combination of ψ and ψ_c would be allowed, since the Dirac mass can be written as $m_d I$, where I is the unit matrix. This is not the case for a charged fermion such as the electron. Mixing ψ and ψ_c would be equivalent to mixing the electron and positron. This cannot happen because of charge conservation. Specifically, charge conservation demands that the Majorana mass M must be zero for charged fermions.

The neutrino is electrically neutral. Charge conservation does not force neutral particles to have a zero Majorana mass term. In a sense then, Majorana neutrinos are more likely than Dirac neutrinos, since any value of M except zero will produce Majorana neutrinos.

2.3 Neutrino Masses in Gauge Theories

In the standard $SU(2)_L \times U(1)$ theory of electro-weak interactions, fermion mass terms cannot appear in the fundamental Lagrangian. These terms would explicitly

break the $SU(2)_L$ gauge symmetry. As a result the Higgs mechanism is used to generate the fermion masses. A coupling of the form $g_f\phi\bar{\psi}\psi$ is assumed, where ϕ is the Higgs field and g_f is the coupling constant. Since the Higgs field has a non-zero vacuum expectation value f, an effective mass $m_f = g_f f$ is generated. The coupling g_f is fixed so that the experimentally measured mass is produced. In the case of the neutrino, no Higgs coupling is assumed and the neutrino is massless.

The Higgs mechanism could generate neutrino mass. This mass would be a Dirac mass of the form,

$$m\bar{\psi}\psi = m(\bar{\psi}_R\psi_L + \bar{\psi}_L\psi_R) \tag{2.6}$$

where

$$\psi = \psi_L + \psi_R \quad \psi_{L(R)} = \frac{1}{2}(1 - (+)\gamma_5)\psi \tag{2.7}$$

The neutrino mass m_ν must be very much smaller than the electron mass m_e or a quark mass m_q. Yet, all these masses are generated by the same Higgs field. There is a good deal of theoretical prejudice against such a wide range of masses being generated by the same process.

The "see saw" mechanism of Yanagida, Gell-Mann, Ramond and Slansky is a mechanism for explaining the small value of a possible neutrino mass [10]. (The presence of a very large matrix element produces very small and very large eigenvalues in the diagonalization process much as a large mass on one side of a "see saw" upsets its balance. Hence the name "see saw".) The (ψ, ψ_c) basis of the previous section is no longer adequate. The fundamental fields are ψ_L and ψ_R and the new basis is of the form $(\psi_L, \psi_R, \psi_{Lc}, \psi_{Rc})$, where the definition of left and right

are the same as above. M and m_d become 2×2 matrices. The unitary matrix U still "diagonalizes" the mass matrix, if the 1s in equation (2.4) become 2×2 unit matrices. The Majorana fields are $N_{R(L)\pm} = \frac{1}{\sqrt{2}}(\psi_{R(L)} \pm \psi_{R(L)c})$. In terms of the Majorana fields $N_{R(L)\pm}$, the result is.

$$\frac{1}{2}(\ \bar{N}_{L+}\ \ \bar{N}_{R+}\ )(m_d + M)\begin{pmatrix} N_{L+} \\ N_{R+} \end{pmatrix} + \frac{1}{2}(\ \bar{N}_{L-}\ \ \bar{N}_{R-}\ )(m_d - M)\begin{pmatrix} N_{L-} \\ N_{R-} \end{pmatrix} \quad (2.8)$$

Since the Dirac mass term connects left and right states (previous paragraph) and the Majorana mass connects left states to left states and right states to right states.

$$m_d = \begin{pmatrix} 0 & m \\ m & 0 \end{pmatrix} \qquad M = \begin{pmatrix} \mu & 0 \\ 0 & M \end{pmatrix} \quad (2.9)$$

The Dirac mass m is assumed to arise from the Higgs mechanism and be on the order of the electron mass. The mass term μ is a left-handed neutrino mass and is set to zero for simplicity. M is the right-handed neutrino mass and is assumed to be much larger than m, since right-handed neutrinos have not been observed and amplitudes from virtual right-handed neutrinos must be suppressed. M must arise from a Higgs type mechanism operating at a much higher energy scale, in order to preserve the gauge symmetry. The matrix $m_d \pm M$ can be diagonalized by a unitary transformation U, with the result,

$$U = \begin{pmatrix} 1 & \alpha \\ -\alpha & 1 \end{pmatrix}$$

$$m_d + M \rightarrow \begin{pmatrix} -m^2/M & 0 \\ 0 & M \end{pmatrix}$$

$$m_d - M \rightarrow \begin{pmatrix} m^2/M & 0 \\ 0 & -M \end{pmatrix}$$

where $\alpha = m/M << 1$. The eigenstates are N_L and N_R, if α is neglected. The mass term becomes.

$$\frac{m^2}{M}(\bar{N}_{L-}N_{L-} - \bar{N}_{L+}N_{L+})/2 + M(\bar{N}_{R+}N_{R+} - \bar{N}_{R-}N_{R-})/2 \qquad (2.10)$$

A left-handed Majorana neutrino is produced with mass $m^2/M \ll m_e$ as desired, along with a very heavy right-handed Majorana neutrino of mass M. This split into a heavy right-handed and light left-handed neutrino is not possible for a Dirac particle. For $m = m_e$ and $M \sim 1$ TeV, the light neutrino mass m_ν is $O(1$ eV). This can be realized for some gauge theories based on $SU(2)_L \times SU(2)_R \times U(1)$ [8].

In the diagonalization of the two matrices $m_d \pm M$, the two eigenvalues appear with opposite sign. This is consequence of their opposite CP parity. In general charge conjugation may not be a symmetry of the Lagrangian. To a good approximation weak interactions are symmetric under CP; and CP conservation is assumed in the above; hence Majorana neutrinos are expected to be CP eigenstates. In particular, it can be shown that the CP phase is $\pm i$ ($N \rightarrow \pm iN$ under CP) [11]. Consider the case of a Dirac neutrino. $m_d \pm M \rightarrow m_d$. The 2×2 matrix m_d (equation (2.9)) can be diagonalized by the unitary transformation of equation (2.4). The eigenvalues are $\pm m$. This implies there are two mass degenerate Majorana neutrinos of opposite CP parity. A Dirac neutrino is a linear combination of two mass degenerate Majorana neutrinos of opposite CP parity.[12]

So far only one flavor of neutrino has been considered. If there is more than one type of neutrino ($\nu_e, \nu_\mu \ldots$), it is possible within the context of the standard model to generate mass term $m_{ij}\bar{\psi}_i\psi_j$ by the Higgs mechanism, where i, j represent different neutrino flavors. Mass terms of this type produce neutrino mixing, where the mass eigenstates are not equal to the weak interaction eigenstates. In general the weak interaction eigenstates are then a linear combination of the mass eigenstates,

$$\begin{aligned} \nu_{eL} &= \sum_i U_{ei}\nu_{iL} \\ \nu_{\mu L} &= \sum_i U_{\mu i}\nu_{iL} \\ &\vdots \end{aligned} \tag{2.11}$$

where ν_j are the mass eigenstates and the L indicates the left states. The coefficients U_i are unitary matrix elements. In a gauge theory which includes right-handed neutrinos,

$$\nu'_{eR} = \sum_i V_{ei}\nu_{iR} \tag{2.12}$$

where similar relations apply for other neutrino flavors. The right and left states are independent [17], hence

$$\langle \nu_{eL} \mid \nu'_{eR} \rangle = \sum_j U_{ej}V_{ej} = 0 \tag{2.13}$$

This has important consequences for the neutrinoless mode of double beta decay (see section 2.5). Further, since a Dirac neutrino is a linear combination of mass degenerate Majorana neutrinos, it can be assumed that all the mass eigenstates are Majorana neutrinos without any loss of generality.

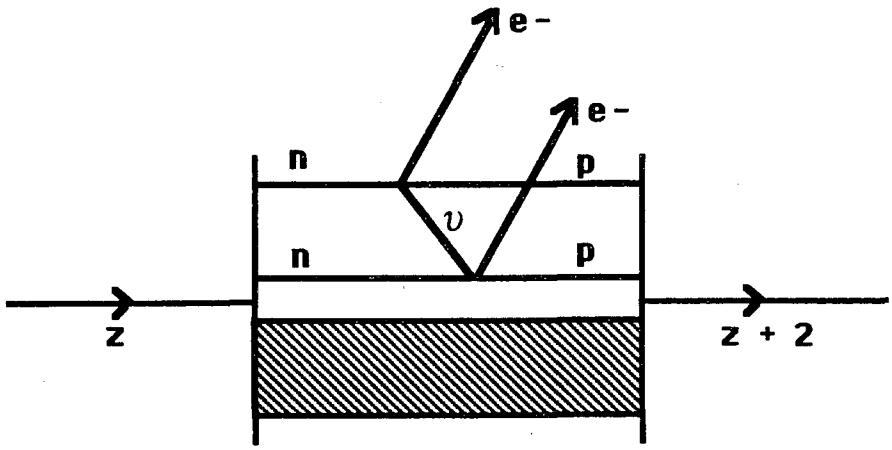

Figure 2.3: **Neutrinoless double beta decay in the 2N model.** The band in the lower half of the diagram represents the spectator nucleons.

2.4 Models for Double Beta Decay

The most commonly encountered model for double beta decay is the two nucleon ($2N$) mechanism. Two neutrons in the initial nucleus undergo ordinary beta decay and transform into two protons of the final nucleus. This is not the same as two separate beta decays because the intermediate nucleus may be virtual. In the neutrinoless mode the neutrino is virtual connecting the two vertices (figure 2.3). This acts as an effective interaction potential between the neutrons. Hadronic currents are treated in the impulse approximation leading to Fermi (τ^+) and Gamow-Teller ($\tau^+\sigma$) nuclear operators. For the electrons only the lowest lying spherical waves (S-waves) are considered in the allowed approximation. Higher spherical waves (P and above) are suppressed because of the long electron wavelength relative to a nuclear radius.

Neutrinoless double beta decay can also occur via nucleon resonances (N^*) inside the nucleus (figure 2.4). Possible reactions are.

$$\Delta^- \Rightarrow p + 2e^-$$

$$\Delta^- \Rightarrow \Delta^+ + 2e^-$$

$$\Delta^\circ \Rightarrow \Delta^{++} + 2e^-$$

As in the $2N$ mechanism a virtual neutrino connects the two vertices in this mode and a $d \rightarrow u$ quark transition occurs at each vertex. The double beta decay amplitudes for the last two reactions are suppressed relative to the first, because of the requirement of an additional strong interaction amplitude to produce the $\Delta \rightarrow p$ transition. In addition, the N^* mechanism does not contribute to the $0^+ \rightarrow 0^+$ ground state transition in the allowed approximation. The hadronic currents must generate both the $0^+ \rightarrow 0^+$ transition and one of the above $\Delta J = 1$ reactions. This cannot occur if both electrons are in S waves or if one electron is in a P wave and the other is in an S wave. As a result this mechanism is highly suppressed relative to the allowed $2N$ process. The N^* mechanism is expected to be of importance in the $0^+ \rightarrow 2^+$ transition [8].

It is possible to induce neutrinoless double beta decay without the mediation of a virtual neutrino. In the Higgs model (figure 2.5), a doublet Higgs boson ϕ is assumed along with triplet Higgs H. The triplet couples to the doublet via $m_H \phi^\dagger H \phi$ and the doublet couples to fermions as $g_f \phi \bar{\psi} \psi$. Since the doublet is responsible for generating the fermion mass and the W boson mass, the quark coupling $g_q \propto \frac{m_q}{M_W}$ and the process is highly suppressed [13].

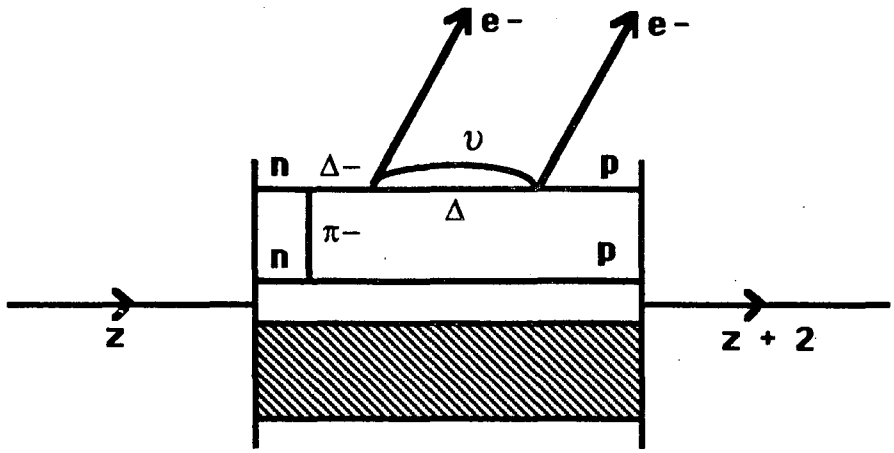

Figure 2.4: **An example of the N* model** of neutrinoless double beta decay.

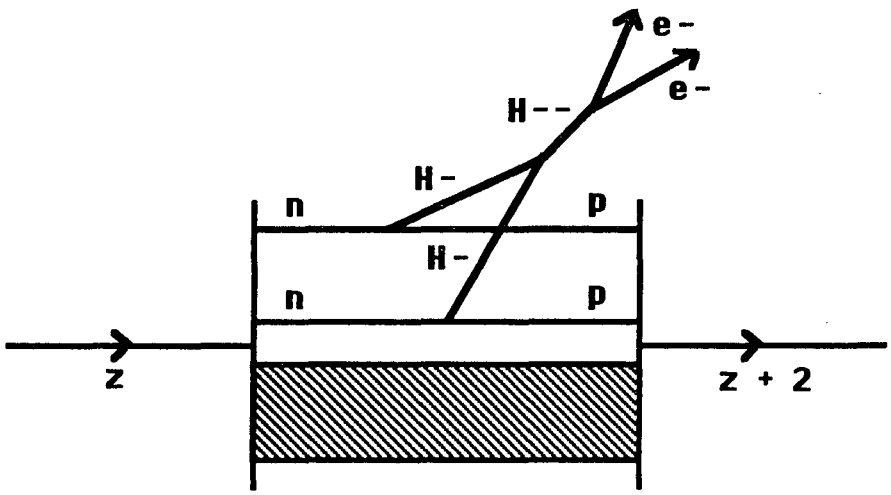

Figure 2.5: **Higgs model** for neutrinoless double beta decay.

Another neutrinoless decay mode, differing from the reaction (1.2), is the majoron process,

$$N^Z \Rightarrow N^{Z+2} + 2e^- + B \tag{2.14}$$

where B is the majoron, a massless Goldstone boson. The majoron is a type of Higgs boson, used to generate neutrino mass and couples to neutrinos via $g\phi\bar{\psi}\gamma_5\psi$. The coupling g may be significant because $g \sim m_\nu/f$, where f, the vacuum expectation value of the majoron field, may be small [14]. The majoron decay may readily be be distinguished from neutrinoless double beta decay by looking at the sum energy spectrum of the two electrons (figure 2.2). Recently, it was reported that this decay mode might be present in ^{76}Ge with a half-life of 6×10^{20} years [15]. Other ^{76}Ge experiments see no evidence for this and set limits on this mode which are inconsistent with the above half-life [16].

2.5 Neutrinoless Double Beta Decay in the 2N Model

An effective interaction hamiltonian for neutrinoless double beta decay is,

$$H_W = \frac{G}{\sqrt{2}}[j_L \cdot (J_L^\dagger + \kappa J_R^\dagger) + j_R \cdot (\eta J_L^\dagger + \lambda J_R^\dagger)] + h.c.$$

where $j_{L(R)}$ and $J_{L(R)}$ are leptonic and hadronic $V-A$ currents ($V+A$ currents), respectively, and $h.c.$ stands for the hermitian conjugate of the preceding terms. κ, η and λ are real constants to be determined by experiment. Double beta decay is a second order process in this effective interaction. Keeping terms to first order

in κ, η and λ generates leptonic contributions to the matrix element of the form $j_L j_L$ and $j_L j_R$. Further, since it can be shown that $j_L j_L \propto m_\nu$ (see below), another small quantity, the κ term is of second order and can be ignored.

In the $SU(2)_L \times SU(2)_R \times U(1)$ gauge model neither η nor λ can be arbitrarily set to zero. This breaks the gauge symmetry. In this model $\lambda \approx (M_{WL}/M_{WR})^2$ and $\eta \approx -\tan(\xi)$, where M_{WL} and M_{WR} are the masses of the left and right gauge boson and ξ is the mixing angle between their mass eigenstates.[8]

The leptonic parts of the amplitude ($j_L j_{L(R)}$) are explicitly of the form,

$$\bar{e}(x)\gamma_\rho(1-\gamma_5)\nu_e(x)\bar{e}(y)\gamma_\sigma(1\pm\gamma_5)\nu_e(y) = \bar{e}(x)\gamma_\rho(1-\gamma_5)\nu_e(x)\nu_e^T(y)(1\pm\gamma_5)\gamma_\sigma^T\bar{e}^T(y) \tag{2.15}$$

where the $(1\pm\gamma_5)$ correspond to the $V\pm A$ currents and the superscript T indicates the transpose. When time ordering is taken into account the $\nu_e(x)\nu_e^T(y)$ terms cancel for a Dirac neutrino and the amplitude is identically zero. For a Majorana neutrino it becomes the standard Feynman propagator times the factor $C = i\gamma_2\gamma_0$. The factor C commutes with γ_5, changes γ_σ^T back to γ_σ and changes $\bar{e}^T(y)$ to $e^C(y)$, where the superscript C indicates the charge conjugate state. The amplitude is then.

$$-i\int \frac{d^4q\ e^{-iq\cdot(x-y)}}{q^2-m_\nu^2}\bar{e}(x)\gamma_\rho(1-\gamma_5)(\gamma\cdot q+m_\nu)(1\pm\gamma_5)\gamma_\sigma e^C(y) \tag{2.16}$$

In terms of the dirac spinors u and v, this is

$$-i\int \frac{d^4q\ e^{-iq\cdot(x-y)}}{q^2-m_\nu^2}\bar{u}(x)\gamma_\rho(1-\gamma_5)(\gamma\cdot q+m_\nu)(1\pm\gamma_5)\gamma_\sigma v(y) \tag{2.17}$$

where q is the virtual neutrino four momentum. For the $j_L j_L$ term, the $\gamma\cdot q$ part of the amplitude vanishes, since γ_5 anticommutes with $\gamma\cdot q$ and $(1-\gamma_5)(1+\gamma_5) = 0$.

The $j_L j_L$ amplitude is proportional to m_ν, as stated above. For the $j_L j_R$ terms, the opposite occurs. The m_ν term is zero and the $\gamma \cdot q$ part is non-zero. This is just a mathematical restatement of the conditions stated in the introduction.

1. The neutrino must be its own antiparticle, a Majorana neutrino.

2. The neutrino must be massive or there must be $V + A$ currents to break helicity conservation.

If neutrino mixing occurs the weak eigenstates are not the same as the mass eigenstates. For each mass eigenstate, factors U_{ei} or V_{ei} (see equations (2.11), (2.12)) appear at each vertex. The $j_L j_L$ amplitude is proportional to $m_i U_{ei}^2$, for each neutrino mass m_i. If neutrino masses are small compared to q, the four momentum ($q \sim O(80 m_e)$ for ^{100}Mo), then the mass can be neglected in the denominator of the propagator in equation (2.17). All amplitudes are then equal up to the factor $m_i U_{ei}^2$. Summing over the neutrinos i, the total $j_L j_L$ amplitude for light neutrinos is proportional to an effective mass $\langle m_\nu \rangle = \sum_i m_i U_{ei}^2$. In the same small mass approximation, the $j_L j_R$ term has an effective couplings $\langle \eta \rangle = \eta \sum_i U_{ei} V_{ei}$ and $\langle \lambda \rangle = \lambda \frac{\cos\theta'}{\cos\theta} \sum_i U_{ei} V_{ei}$, where θ is the standard Cabbibo angle and θ' is the Cabbibo angle for right hadronic currents.

If all neutrinos are light, then in the $SU(2)_L \times SU(2)_R \times U(1)$ gauge model both $\langle \eta \rangle$ and $\langle \lambda \rangle$ are zero, by equation (2.13). To be more precise, the $j_L j_R$ amplitude is non-zero to the extent that neutrino masses are not negligible compared with the four momentum q in the neutrino propagator. If all masses are zero the $j_L j_R$ amplitude vanishes identically. The effective couplings $\langle \eta \rangle$ and $\langle \lambda \rangle$ are useful if the

neutrino mass spectrum can be divided into heavy ($m_\nu \gg q$) and light neutrinos as in the "see saw" mechanism. The contributions from the heavy neutrinos are neglected because the m_ν^2 in the denominator of the propagator suppresses these terms. The sums over i in $\langle\eta\rangle$ and $\langle\lambda\rangle$ are not complete and the effective couplings are non-zero, but may be much smaller than η or λ.

It would seem that the above gauge model also requires massive neutrinos for the $V+A$ mechanism to work. This occurs because the $j_L j_R$ amplitude for a single Majorana neutrino violates unitarity at high energies (electron energies $\rightarrow \infty$). This limit is important because the $j_L j_R$ amplitude is also responsible for the reaction $W^-W^- \rightarrow e^-e^-$. Gauge theories have the general property that they are renormalizable and that unitarity is not violated. As a consequence, in the high energy limit, which is the same as the limit in which all neutrinos are massless, the amplitudes for different neutrinos must cancel each other.

The argument can be extended to general gauge theories, if it is assumed that there is no doubly charged boson, as in the Higgs mechanism of section 2.4. Neutrinoless double beta decay is then mediated only by virtual neutrinos and the $j_L j_R$ amplitude will violate unitarity in the high energy limit unless $\sum_i U_{ei}V_{ei} = 0$. Since the high energy limit is the same as the condition that all neutrinos are massless, the $V+A$ contribution is zero unless at least one neutrino is massive.[17] Given these qualifications the conditions listed above can be combined.

- Neutrinoless double beta decay can occur only if there exists at least one massive Majorana neutrino.

Cancelation can also occur in the effective mass term. Because of the symmetry in equation (2.15), $U_{ei}^2 \neq |U_{ei}|^2$. In the CP conserving case $\langle m_\nu \rangle = \sum_k m_k U_{ek}^2 = \sum_k \frac{\chi_k}{i} \mid U_{ek} \mid^2 m_k$, where χ_k is the CP phase $(\pm i)$[18]. In the case of a Dirac neutrino the sum extends over two mass degenerate Majorana neutrinos of opposite CP parity, $\langle m_\nu \rangle = (m_1 - m_2)/2 = 0$, as expected.

Because of cancellations in the various sums, it is possible for the contribution of the light neutrinos to be negligible compared to that of the heavy neutrinos $(m \gg q)$. This is the exact opposite of what has been assumed up to this point. In equation (2.17), q can neglected relative to m_ν in the denominator of the neutrino propagator. The $q \cdot \gamma$ term of the numerator is of order q/m_ν and can be dropped relative to the m_ν term; hence only the $j_L j_L$ contribution is important. The amplitude is then proportional to $1/m_\nu$. If neutrino mixing is added, this becomes an effective inverse mass $\langle 1/m_\nu \rangle = \sum_j U_{ej}^2/m_j$.

2.5.1 The Neutrino Mass Mechanism

In treating the hadronic part of the matrix element, only the m_ν term $(j_L j_L J_L^\dagger J_L^\dagger)$ will be considered in detail. The hadronic amplitude is calculated in non-relativistic perturbation theory. It is,

$$\sum_a \frac{\langle N_f \mid J_{L\rho}^\dagger(x) \mid N_a \rangle \langle N_a \mid J_{L\sigma}^\dagger(y) \mid N_i \rangle}{(E_a + \omega + \varepsilon_1 - M_i)} \tag{2.18}$$

where N_i and N_f are the initial and final nuclear states with masses M_i and M_f. ω and ε_1 are respectively the neutrino and the electron (emitted at y) energies. The sum is over all intermediate nuclear states N_a, with energies E_a. The closure ap-

proximation is routinely used to calculate this quantity. The intermediate nuclear state energies E_a are replaced by an average value μ. The sum over intermediate states becomes the identity operator. The amplitude is

$$\frac{S_{\rho\sigma}(x,y)}{(\mu+\omega+\varepsilon_1-M_i)} = \frac{\langle N_f \mid J^\dagger_{L\rho}(x)J^\dagger_{L\sigma}(y) \mid N_i\rangle}{(\mu+\omega+\varepsilon_1-M_i)} \tag{2.19}$$

Since ω is larger than average nuclear excitation energies, such as the giant Gamow-Teller resonance, the variation of the energy denominator with E_a is weak and this approximation is justified.

In order to conform to the non-relativistic perturbation theory used in the hadronic term, the neutrino propagator has to be integrated over dq_0. If light neutrinos are assumed to dominate the process, the leptonic part becomes.

$$-i\langle m_\nu\rangle \int \frac{d^3\mathbf{q}}{\omega} e^{i\mathbf{q}\cdot(x-y)}\bar{u}(x)\gamma_\rho\gamma_\sigma(1+\gamma_5)v(y) = -i\langle m_\nu\rangle \int \frac{d^3\mathbf{q}}{\omega} e^{i\mathbf{q}\cdot(x-y)}t_{\rho\sigma}(x,y) \tag{2.20}$$

This must be contracted with the hadronic part and appropriately anti-symmetrized with respect to the two final state electrons. The result is

$$-i\langle m_\nu\rangle \int \frac{d^3\mathbf{q}}{\omega} S^{\rho\sigma}(x,y)[\frac{t_{\rho\sigma}(x,y)e^{i\mathbf{q}\cdot(x-y)}}{(\mu+\omega+\varepsilon_1-M_i)} - \frac{t_{\rho\sigma}(y,x)e^{i\mathbf{q}\cdot(y-x)}}{(\mu+\omega+\varepsilon_2-M_i)}] \tag{2.21}$$

(Summation over repeated indices is implicit in this formula.) Because of the symmetry properties of S and t under the combined operation $x \leftrightarrow y$ and $\rho \leftrightarrow \sigma$[8], this becomes,

$$-i\langle m_\nu\rangle \int \frac{d^3\mathbf{q}}{\omega} e^{i\mathbf{q}\cdot(x-y)}S^{\rho\sigma}(x,y)t_{\rho\sigma}(x,y)[\frac{1}{(\mu+\omega+\varepsilon_1-M_i)} + \frac{1}{(\mu+\omega+\varepsilon_2-M_i)}] \tag{2.22}$$

where the integration variable $\mathbf{q}$ has been replaced by $-\mathbf{q}$ in the second term in order to factor out the exponential. In addition, $S^{\rho\sigma}$ is symmetric under interchange of ρ and σ. Therefore, only the symmetric part of $t_{\rho\sigma}$ under this operation contributes to the sum. The tensor properties of $t_{\rho\sigma}$ are determined by $\gamma_\rho\gamma_\sigma$. The symmetric part is $(\gamma_\rho\gamma_\sigma+\gamma_\sigma\gamma_\rho)/2 = g_{\rho\sigma}$. The electronic and hadronic contributions then factor out.

$$S^{\rho\sigma}t_{\rho\sigma} = S^{\rho}_{\rho}t; \quad t = \bar{u}(x)(1+\gamma_5)v(y) \tag{2.23}$$

The neutrino propagator term along with the two energy denominators defines an effective interaction potential $h(x,y)$ after integration over the virtual neutrino momentum $\mathbf{q}$,

$$h(x,y) = \frac{\phi(\bar{E}r)R}{r} \simeq \frac{Re^{-1.5\bar{E}r}}{r}; \quad r = \mid x-y \mid \tag{2.24}$$

where $\bar{E} = \mu - (M_i + M_f)/2$, the weak dependence on ε_1 and ε_2 has been dropped and R, the nuclear radius, has been introduced to make $h(r)$ dimensionless. (A factor of $1/R^2$ must be included in the decay rate formula to compensate.) For r on the order of a nuclear radius the exponential is approximately equal to unity and $h(r) \approx \frac{R}{r}$. The hadronic currents are treated in the impulse approximation leading to Fermi and Gamow-Teller nuclear operators.

$$J^\dagger = (\frac{g_V}{g_A}\sum_i \tau_i^+, \sum_j \tau_j^+ \boldsymbol{\sigma}_j) \tag{2.25}$$

The sum extends over all nucleons i in the initial or final state and the factor $\frac{g_V}{g_A}$ accounts for the fact that hadronic currents are not pure $V-A$ due to strong interaction effects. τ^+ is the isospin raising operator ($n \rightarrow p$) and $\boldsymbol{\sigma}$ is the Pauli

spin matrix three vector. In the allowed approximation of ordinary beta decay the x dependence of the electron wavefunction is ignored, since the electron wavelength is much larger than a nuclear radius. Using this approximation for both electrons and integrating over x and y, the contraction S_ρ^ρ along with the neutrino potential $h(x,y)$ generates double Fermi and double Gamow-Teller matrix elements.

$$\begin{aligned} \int d^3x d^3y h(x,y) S_\rho^\rho &= \frac{g_V^2}{g_A^2} M_F - M_{GT} \qquad (2.26) \\ M_F &= \langle N_f(x) \mid h(x,y) \sum_{ij} \tau_i^+ \tau_j^+ \mid N_i(y) \rangle \\ M_{GT} &= \langle N_f(x) \mid h(x,y) \sum_{ij} \boldsymbol{\sigma}_i \cdot \boldsymbol{\sigma}_j \tau_i^+ \tau_j^+ \mid N_i(y) \rangle \end{aligned}$$

The integrations over x and y are implicit in the definitions of M_F and M_{GT}. The $i = j$ term is excluded in all sums.

The decay rate is obtained by squaring the amplitude and integrating over phase space. If free particle spinors are used for the electron wavefunctions, the electron contribution to the amplitude squared is $t^2 \propto (1 - \beta_1 \beta_2 \cos\theta)$, where β_1 and β_2 are the electron velocities and θ is the angle between the two electrons. Coulomb correction factors must be included for each electron. They can be approximated by the form $F(Z)/\beta$, where $F(Z)$ is a function of the nuclear charge Z only. The phase space factor is $p_1 \varepsilon_1 p_2 \varepsilon_2 d\varepsilon_2$ after energy conservation is used to eliminate the ε_1 integration. The electronic contribution to the rate is,

$$F(Z)^2 \varepsilon_1^2 \varepsilon_2^2 d\varepsilon_2 (1 - \beta_1 \beta_2 \cos\theta) d\Omega; \quad \varepsilon_1 = Q - \varepsilon_2 \qquad (2.27)$$

where Q is the energy difference between the initial and final nuclear states. Upon integration over the solid angle the one electron energy spectrum is obtained (figure 2.6).

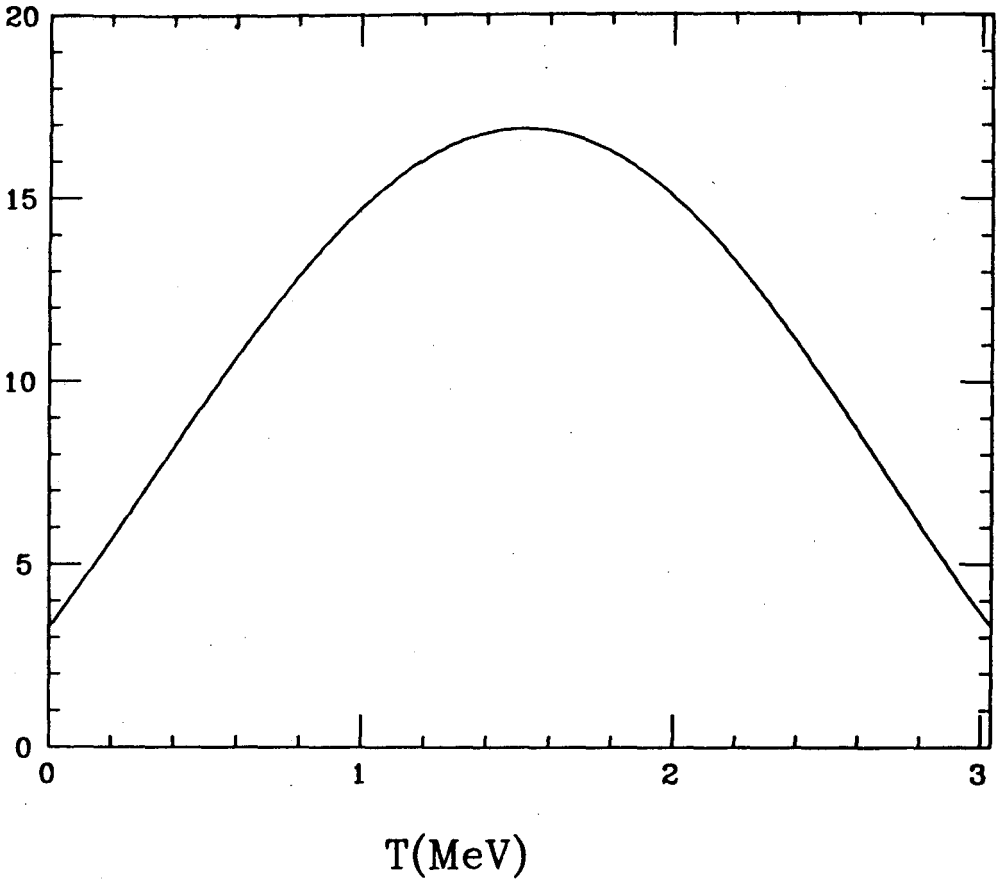

Figure 2.6: **One electron energy spectrum for ^{100}Mo** . The vertical scale is arbitrary.

The maximum occurs at the midpoint. The endpoints are non-zero because of the coulomb correction. Integration over the remaining electron energy can be done analytically, if the $\beta_1\beta_2$ term is ignored. This generates a fifth order polynomial in the decay energy Q and the electron mass m_e, $P(Q, m_e)$.[19]. To leading order the decay rate is proportional to Q^5. The inverse half-life is then,

$$\frac{1}{\tau^{0\nu}_{1/2}} = \frac{G^4}{R^2} P(Q, m_e) F(Z)^2 \mid M_{GT} - \frac{g_V^2}{g_A^2} M_F \mid^2 \langle m_\nu \rangle^2 \tag{2.28}$$

where G is the Fermi coupling. (All numerical factors are incorporated into the definition of $P(Q, m_e)$.)

Use of the free particle spinors and the above form of the coulomb correction produces the correct angular correlation and approximates the one electron spectrum reasonably well, but badly underestimates the total decay rate. Exact solutions of the Dirac equation for an electron in the field of a nucleus must be used and the phase space integration must be done numerically. The results are summarized in terms of an integrated kinematical factor $\mathcal{G}(Q, Z)$. The inverse half-life becomes,

$$\frac{1}{\tau^{0\nu}_{1/2}} = \mathcal{G}(Q, Z) \mid M_{GT} - \frac{g_V^2}{g_A^2} M_F \mid^2 \langle m_\nu \rangle^2 \tag{2.29}$$

where all constants, including G^4 and R^2 are included in the definition of $\mathcal{G}(Q, Z)$. $\mathcal{G}(Q, Z)$ has been calculated by Doi et.al.[8] for most isotopes of interest. Many of these values can also be found in Engel et.al. [20].

Both the double Fermi and double Gamow-Teller nuclear operators are scalars under rotation. As a result only the $0^+ \rightarrow 0^+$ transition is allowed. This is a consequence of the closure and allowed approximations. Implicit in ignoring the

position dependence of the electron wavefunctions in the allowed approximation is the assumption that both electrons are in spherical S waves. If P waves are considered, factors of $p \cdot (x - y)$ would appear in the nuclear matrix element. If one electron is in a P wave and the other is in an S wave, a $0^+ \rightarrow 1^-$ transition could occur, but there are no low lying 1^- nuclear final states. To reach a 1^+ final state, both electrons would have to be in P waves. This is possible but the rate would be highly suppressed.

If closure is not used then the 1^+ transition can occur with both electrons in S waves. This is best understood by considering angular momentum conservation. The two electron spins add up to 0 or 1. The initial nucleus is 0^+. As a result, angular momentum conservation demands the final state be 0^+ or 1^+. In terms of nuclear operator, the 1^+ transition requires the inclusion of products of Fermi and Gamow-Teller operator $(\tau_i^+ \tau_j^+ \sigma_j)$. Operators of this type exist if closure is not used. The double S wave 1^+ transition is suppressed to the extent that the closure approximation is accurate.

Similar considerations explain the $(1 - \beta_1 \beta_2 \cos\theta)$ angular correlation. Each electron is generated by the $V - A$ interaction. As a consequence both electrons have dominant left-handed helicities. In the allowed approximation both electrons are in S waves and their total spin must be zero for the $0^+ \rightarrow 0^+$ transition (which is the only transition in the closure approximation). With the same helicities the electrons must be emitted predominantly in opposite directions in order to cancel their spins; hence the above angular correlation.

Almost all of the above discussion remains unchanged if heavy neutrinos dom-

inate the decay. The only difference is the neutrino potential (equation (2.24)), which now becomes the point interaction $h(x,y) = 2\pi\delta^3(x-y)/m_\nu^2$. This generates different double Fermi and double Gamow-Teller matrix elements,

$$\begin{aligned} M_F' &= \langle N_f(x) \mid \sum_{ij} \tau_i^+ \tau_j^+ \mid N_i(x) \rangle \\ M_{GT}' &= \langle N_f(x) \mid \sum_{ij} \boldsymbol{\sigma}_i \cdot \boldsymbol{\sigma}_j \tau_i^+ \tau_j^+ \mid N_i(x) \rangle \end{aligned} \tag{2.30}$$

where there is only one integration over x. The inverse half-life is

$$\frac{1}{\tau_{1/2}^{0\nu}} = 4\pi^2 R^2 \mathcal{G}(Q,Z) \mid M_{GT}' - \frac{g_V^2}{g_A^2} M_F' \mid^2 \left\langle \frac{1}{m_\nu} \right\rangle^2 \tag{2.31}$$

where $\langle \frac{1}{m_\nu} \rangle$ is the effective inverse mass mentioned previously and R is the nuclear radius. Angular correlations, selection rules, the single electron spectrum and $\mathcal{G}(Q,Z)$ remain the same.

2.5.2 The Right-Handed Current Mechanism

The $V+A$ current contributes to the amplitude only for light neutrinos. The leptonic contribution is proportional to $\gamma \cdot q$. This can be broken down into two parts, a scalar term, $\gamma_0 \omega$ and a vector term, $\boldsymbol{\gamma} \cdot \mathbf{q}$.

The scaler part is very much like the massive neutrino term just considered. Differences arise because of the symmetry properties of the electronic amplitude $t_{\rho\sigma}$. There is no sign change on the second energy denominator term as in equation (2.22). The energy denominator is.

$$\frac{1}{(\mu+\omega+\varepsilon_1-M_i)} - \frac{1}{(\mu+\omega+\varepsilon_2-M_i)} = \frac{\varepsilon_1-\varepsilon_2}{(\mu+\omega+\varepsilon_1-M_i)(\mu+\omega+\varepsilon_2-M_i)} \tag{2.32}$$

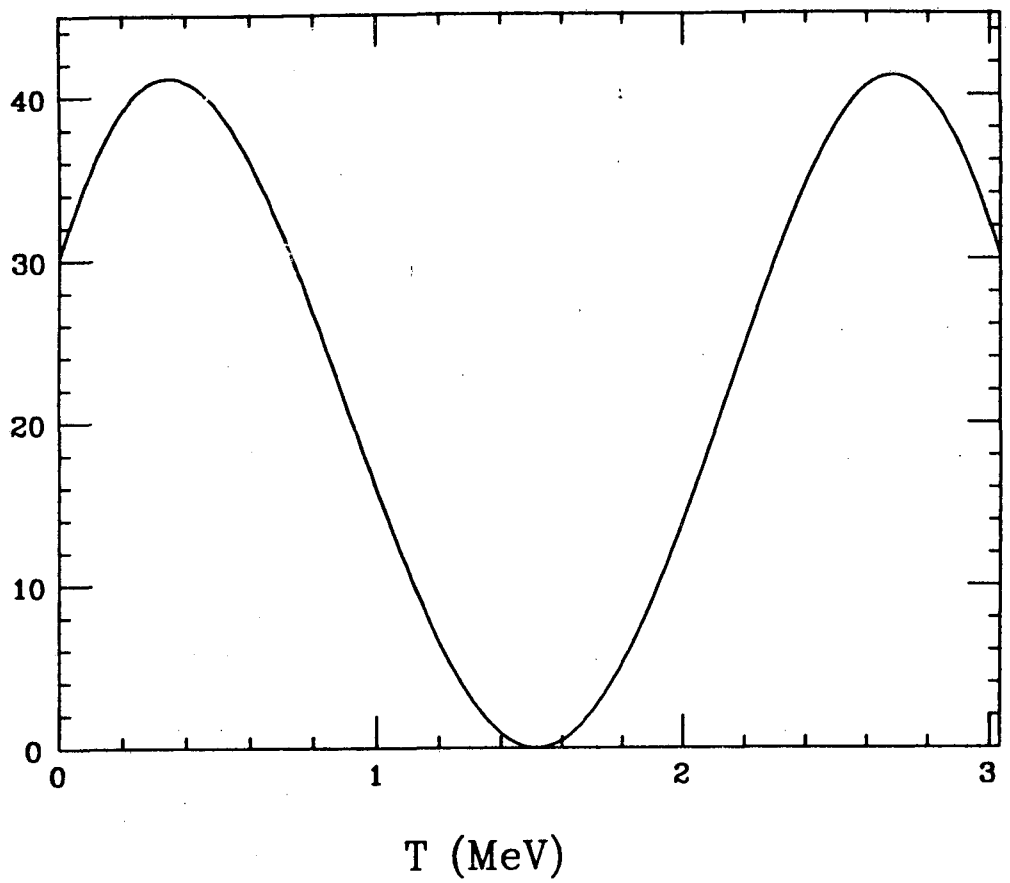

Figure 2.7: **One electron energy spectrum for ^{100}Mo** , given that the RHC scalar term dominates. The vertical scale is arbitrary.

If this is the dominant term a factor of $(\varepsilon_1 - \varepsilon_2)^2$ must be included in the decay rate. As a result the one electron spectrum is no longer dominated by phase space and becomes bimodal (figure 2.7). The spectrum will go to zero at the midpoint only if all other parts of the amplitude are identically zero. Integrating over this spectrum produces, to leading order, a Q^7 energy dependence for the total decay rate, but as before the integration must be done numerically to insure accuracy. The neutrino potential also changes because the denominator on the right above is

used to produce it. The nuclear matrix elements (equations (2.26)) are still double Fermi and double Gamow-Teller, but with the new potential $h'(x,y)$. Selection rules are the same as before. Only the $0^+ \rightarrow 0^+$ transition is allowed to leading order.

The vector term, $\boldsymbol{\gamma}\cdot\mathbf{q}$, also generates a different neutrino potential. The energy denominators are the same as in the neutrino mass case because of the substitution $\mathbf{q} \rightarrow -\mathbf{q}$ required to factor out the exponential in the second term (see equation (2.22)). If the vector term is dominant the single electron energy spectrum and Q^5 rate dependence are the same as in the neutrino mass case. The difference in the potential arises from the $\boldsymbol{\gamma}\cdot\mathbf{q}$ term itself. Integration over $\mathbf{q}$ generates a factor of $\mathbf{r}$ in the numerator of the neutrino potential. The closure approximation does generate double Fermi and double Gamow-Teller type nuclear operators, but in addition there are factors of $\boldsymbol{\sigma}\cdot\mathbf{r}$ to be considered. This operator is odd under parity. To conserve parity in the $0^+ \rightarrow J^+$ transitions one electron must be in a spherical P wave. As a consequence transitions to all possible final states ($J^P = 0^+, 1^+, 2^+$) are allowed in lowest order for this term. This is the only term which allows the $0^+ \rightarrow 2^+$ transition in lowest order. Observation of neutrinoless double decay to the 2^+ excited state would be clear evidence for the existence of right-handed currents.

For both the scaler and vector part of the $V+A$ term, both final state electrons are emitted with predominantly opposite helicities. In the ground state transition, ($0^+ \rightarrow 0^+$) angular momentum conservation demands that electrons have no angular momentum. In the plane formed by the two electron trajectories, only the

electron spins contribute to this component of the angular momentum. The spins must tend to cancel, so that it is expected that the two electrons will be emitted predominantly in the same direction to cancel their opposite helicities. The angular correlation is then $(1 + \beta_1\beta_2 \cos\theta)$.

2.5.3 The Total Decay Rate Formula

If nuclear recoil is included, the vector part of the $V + A$ term contributes five nuclear matrix elements to the $0^+ \rightarrow 0^+$ transition. The neutrino mass term and the scalar part of the $V + A$ term each contribute a double Fermi and double Gamow-Teller nuclear matrix element. If all terms contribute there are nine nuclear matrix elements, the total decay rate becomes for light neutrinos[8],

$$\begin{aligned} R_{0\nu}(0^+ \rightarrow 0^+) &= C_1 \left(\frac{\langle m_\nu \rangle}{m_e}\right)^2 + C_2 Re\left(\frac{\langle m_\nu \rangle}{m_e}\langle\lambda\rangle\right) + C_3 Re\left(\frac{\langle m_\nu \rangle}{m_e}\langle\eta\rangle\right) \\ &\quad + C_4\langle\lambda\rangle^2 + C_5\langle\eta\rangle^2 + C_6 Re\left(\langle\lambda\rangle\langle\eta\rangle\right) \end{aligned} \tag{2.33}$$

where Re stands for the real part of the quantity in parenthesis. This is done because the effective couplings may be complex. The six coefficients C_i are defined in Doi et.al.[8] and depend on the nine nuclear matrix elements and nine integrated kinematical factors. These kinematical factors vary between the fifth and seventh power of the energy release as mentioned in the previous two subsections and are a strong function of Z, the nuclear charge.

Reference	^{76}Ge	^{82}Se	^{100}Mo
Engel et.al. [20]	1.97	1.48	2.8
Tomoda et.al [21]	4.35	3.93	—
Grotz et.al [22]	12.9	10.1	—
Haxton et.al [7]	5.02	4.06	—

Table 2.1: $\mid \mathbf{M_{GT}} - \frac{\mathbf{g_V^2}}{\mathbf{g_A^2}}\mathbf{M_F} \mid$ The combination of nuclear matrix elements appropriate for the neutrino mass mechanism of neutrinoless double beta decay. A dash indicates that this group has not done the calculation for the element in question.

2.5.4 Nuclear Matrix Elements

Of the nine nuclear matrix elements in the ground state decay rate formula for light neutrinos, only two, the double Fermi and double Gamow-Teller matrix elements appropriate for the neutrino mass mechanism, have been calculated for ^{100}Mo . Table 2.1 lists the total matrix element for the neutrino mass mechanism of double beta decay for three selected isotopes as calculated by various authors. The conventions of references [20] and equation (2.29) are used. The Caltech group of Engel et.al. has done the only ^{100}Mo matrix element calculations to date. As Table 2.1 shows, there is as much as a factor of 7 disagreement between calculations by different groups for the same isotope. Similar disagreements occur in other isotopes and matrix elements.

These discrepancies have occurred because of the complexities of the calcula-

tions. Detailed models of both the initial and final state nucleus must be used and various approximation schemes employed. The Caltech group of Engel et.al. uses the Quasiparticle Random Phase Approximation (QRPA) to calculate matrix elements. The results of their calculations depend strongly on a particle-particle interaction strength parameter, α. The value of α is determined by an examination of β^+ decay, but only to an accuracy of $\pm 5\%$. The Caltech values in Table 2.1 correspond to the lower limit of the allowed range of α. Using the upper limit reduces the ^{76}Ge and ^{82}Se values by a factor of 2. In ^{100}Mo the QRPA breaks down for the final state Ru nucleus at this value of α and a matrix element calculation is not possible. The Tübingen group of Tomoda et.al. also uses QRPA, but finds their neutrinoless matrix elements to depend only weakly on α and quote only single values rather than a range of values. The calculations of both Grotz et.al. and Haxton et.al are parameter free. Grotz et.al. uses QRPA, but ignores the particle-particle interaction. Haxton et.al. does a full shell model calculation.

The only way of testing the various approximation schemes used in matrix element calculations is by comparison of predicted two neutrino decay half-lives with existing experimental values. Experimental results are listed in Table 2.2. Table 2.3 lists predicted half-lives for these isotopes, calculated by the same authors as above. The Caltech calculations of Engel et.al. are again parameter dependent with the values for the lower limit of α listed. The half-life is a factor of 10 and 5 smaller for ^{82}Se and ^{130}Te, respectively, at the upper limit of α. Unlike their neutrinoless calculations, the Tübingen group [23] (not listed in Table 2.3) finds that the two neutrino matrix element goes through zero within the allowed range of

Reference	^{82}Se	^{130}Te
Elliot et.al. [6]	$(1.1 + .6 - .3) \times 10^{20}$	—
Kirsten et.al [4]	$(1.3 \pm .05) \times 10^{20}$	$(1.5 - 2.75) \times 10^{21}$
Manuel et.al [5]	$(1.0 \pm .4) \times 10^{20}$	$(7 \pm 2) \times 10^{20}$

Table 2.2: **Experimental $\tau_{1/2}(2\nu)$** Measured half-lives, in years, for two neutrino double beta decay. A dash indicates that no measurement on this isotope was done. The first measurement is by a direct counting experiment. All other are geochemical.

the particle-particle strength parameter. They therefore can only put a lower limit on the half-life. The limits they set are all consistent with the experimental values in Table 2.2. Of the results listed in Table 2.3, the calculations of Engel et.al. come closest to the experimental numbers. The ^{82}Se calculation is essentially identical to the experimental value, but the ^{130}Te result is still considerably in error.

To set the scale for neutrinoless double beta decay, the matrix elements in Table 2.1 of Engel et.al. are used in equation (2.29) to calculate the half-lives. For an effective majorana neutrino mass, $\langle m_\nu \rangle$, of 1 eV, the results are 2.7×10^{25}, 1.1×10^{25} and 1.9×10^{24} years for ^{76}Ge, ^{82}Se and ^{100}Mo , respectively. These half-lives differ mostly because of the strong dependence of the integrated kinematical factor on Z and Q. Given the variation in Table 2.1, the above values may be lower by as much as a factor of 50.

Reference	^{82}Se	^{130}Te
Engel et.al. [20]	1.2×10^{20}	2.2×10^{20}
Grotz et.al [22]	1.5×10^{19}	1.2×10^{20}
Haxton et.al [7]	2.6×10^{19}	1.7×10^{19}

Table 2.3: **Theoretical** $\tau_{1/2}(2\nu)$ Half-life predictions, in years, for two neutrino double beta decay by various authors.

2.6 Previous Experiments

One of the earliest experiments on ^{100}Mo was done by Winter [24] in 1955. Using a Wilson cloud chamber and ordinary Mo foils, a limit of 3×10^{17} years was placed on the total half-life, including all modes. At the time, this experiment and others like it were taken as proof that the neutrino was a Dirac particle, since the neutrinoless decay induced by Majorana neutrinos was expected to occur with a half-life on the order of 10^{13} years and the two neutrino decay which is allowed for both Dirac and Majorana neutrinos had an estimated half-life of 10^{21} years. With the advent of parity violation in ordinary beta decay and the introduction of the $V-A$ interaction it slowly became clear that this conclusion was wrong, since the helicity requirements of the $V-A$ structure of the weak interaction could strongly suppress the neutrinoless reaction if the neutrino were nearly massless.

For many years geochemical experiments dominated the field and provided the best double beta decay limits. In this technique ore samples rich in candidate

double beta decay elements are K-Ar dated and the number of double beta decay daughter nuclei is measured using a mass spectrometer. This procedure is made possible by the high sensitivity of noble gas mass spectrometers. Since the decay products of the ^{82}Se and Te isotopes are Kr and Xe respectively, these double beta decay candidates are particularly suited to this technique. The measurements of references [4] and [5] in Table 2.2 were done using this method.

Geochemical experiments cannot distinguish between decay modes. Only direct counting experiments which detect the individual events can do so. Revival of interest in direct counting experiments on double beta decay occurred with the advent of GUTS in the 1970s. One of the most popular techniques was pioneered by the Milan group headed by Fiorini. A Ge solid state detector is used both as the source material and as the detector. Naturally occurring Ge is 7.8% ^{76}Ge, a double beta decay candidate. The technique is essentially electron calorimetry. One searches for the neutrinoless decay mode by looking for a peak in the energy spectrum at the Ge decay energy of 2.045 MeV. The detectors have excellent energy resolution with a full width of approximately 3 keV. Ge detectors are also very pure. As a consequence they are low in radioactive contamination which can mimic double beta decay. Current Ge experiments are listed in Table 2.4, along with other experiments which have produced limits on the ground state transition of neutrinoless double beta decay. All of the Ge experiments are operating underground in order to reduce cosmic rays as background sources.

In attempt to go beyond simple calorimetry and achieve better background rejection capabilities, many of the Ge groups in Table 2.4 use active NaI shields

Group	Isotope	Detector	Mole-years	$\tau_{1/2}$
Zar./Bord./Stras. [25]	^{76}Ge	Ge*	.68	.2
CIT/SIN/Neu. [25]	^{76}Ge	Ge*	.40	.6
Osaka [26]	^{76}Ge	Ge*	.93	.7
PNL/USC [25]	^{76}Ge	Ge	.71	1.4
Quelph/Apt./Que. [25]	^{76}Ge	Ge	1.2	1.6
Milan [25]	^{76}Ge	Ge	3.0	1.8
UCSB/LBL [25]	^{76}Ge	Ge*	9.0	5.0
UCI [27]	^{82}Se	TPC	.15	.11
Osaka [26]	^{100}Mo	Si*	.007	.002
Kiev [28]	^{100}Mo	PS	.61	.021
Milan [29]	^{136}Xe	MPC	.070	.017 (90%)

Table 2.4: **Experimental Lower Limits on $\tau_{1/2}(0\nu)$.** All limits are in unit of 10^{23} years (68% c.l. unless noted otherwise). Ge=Ge solid state detector, TPC=Time Projection Chamber, Si=Si solid state detectors, PS=Plastic Scintillator, MPC=Multi-element Proportional Chamber and *=active NaI shield.

in anticoincidence with their Ge detectors. The problem is that the NaI has introduced about as much background as the shield rejects, with the result that the Ge groups with the best limits have about the same background per unit mass of Ge, even though one uses a NaI shield and the others do not.

The only direct counting experiment which has succeeded in making a measurement of double beta decay is the ^{82}Se experiment at UCI. Their two neutrino result (Elliot, et.al. [6], Table 2.2) confirms the geochemical work. Table 2.4 lists their neutrinoless limit. This group uses a Time Projection Chamber (TPC). The ^{82}Se source material is formed into a thin sheet and placed in the central plane of the the TPC. A 700 gauss magnetic field is used to identify the particles as electrons. The requirement that the two electron vertex originates at the source plane greatly reduces backgrounds. The energy resolution for two 1 MeV electrons is .25 MeV. Because of accessibility requirements the detector is operated at sea level with a cosmic ray veto. The main sources of background in this system are beta decay followed by internal conversion in the source material and Møller scattering of electrons in the source. The origin of the electrons which Møller scatter can either be beta decays or Compton scattering of gamma rays in the source plane. The main drawback for this system is size and complexity, which does not allow for the use of a large quantity of source material and will not allow the experiment to be operated conveniently underground.

The most recent experiment on ^{100}Mo was done by the Osaka group in Table 2.4. This group used a technique almost identical to our own. Foils of isotopically separated ^{100}Mo are placed between Si solid state detectors. The simplicity of

the design tends to minimize possible sources of radioactive contamination. The segmentation however provides more information than a single crystal Ge experiment, facilitating background rejection. Their design differs from our own mainly in the size and properties of the Si detectors used. Their detectors are smaller in diameter (2 in. versus our 3 in.) and are thicker (.5 cm versus our .14 cm). Their Si detectors also have a 15 μm dead layer on one side, whereas our's have almost no dead layer in comparison (see section 3.1). These differences affect the experiments energy resolution and background rejection capabilities. The Osaka group found contamination from the ^{238}U and ^{232}Th radioactive decay chains at the 100 ppb level in their ^{100}Mo foil. Their limit on the neutrinoless half-life is 2×10^{20} years.

The best previous limit on ^{100}Mo comes from an experiment by the Kiev group in Table 2.4. This experiment used plastic scintillator and separated ^{100}Mo foils. The radioactive contamination in this experiment was comparable to that of the Osaka group, but the sample size was much larger. Their limit placed on neutrinoless double beta was 2×10^{21} years.

Listed at the bottom of Table 2.4 are preliminary results from a new ^{136}Xe experiment done by the Milan group. The new experiment uses a Multi-element Proportional Chamber (MPC) filled with Xe gas. The system conservatively has an energy resolution of 5% . The chamber holds 100 liters of Xe at a pressure of approximately 10 atmospheres. In the future the Milan group plans to use enriched Xe with a 60% isotopic abundance of ^{136}Xe.

Chapter 3

Description of the Experiment

In this experiment an array of 40 solid state Si detectors is used to look for the neutrinoless double beta decay of ^{100}Mo. The Si detectors are disks with a thickness of 1.4 mm and a diameter of 7.6 cm. Each detector is separated from the next by a gap of 1 mm, creating a cylindrical stack of detectors 9.5 cm high (figure 3.1). Thin Mo films are placed in the 1 mm gap between the Si detectors.

At first, this technique may seem similar to previous Ge experiments, simply another attempt at electron calorimetry. This is not the case. Most double beta decays deposit energy in more than one detector. The spatial distribution of energy among the detectors in the array is a useful tool in distinguishing double beta decay from background. Specifically, events with energy in only one detector and events with energy in a discontiguous set of detectors can be eliminated. Above an energy of 2 MeV, the one-detector events are predominantly alpha particles and have only a small probability of being double beta decay events. The discontiguous events are caused by beta-gamma and alpha-gamma cascades within the Si stack

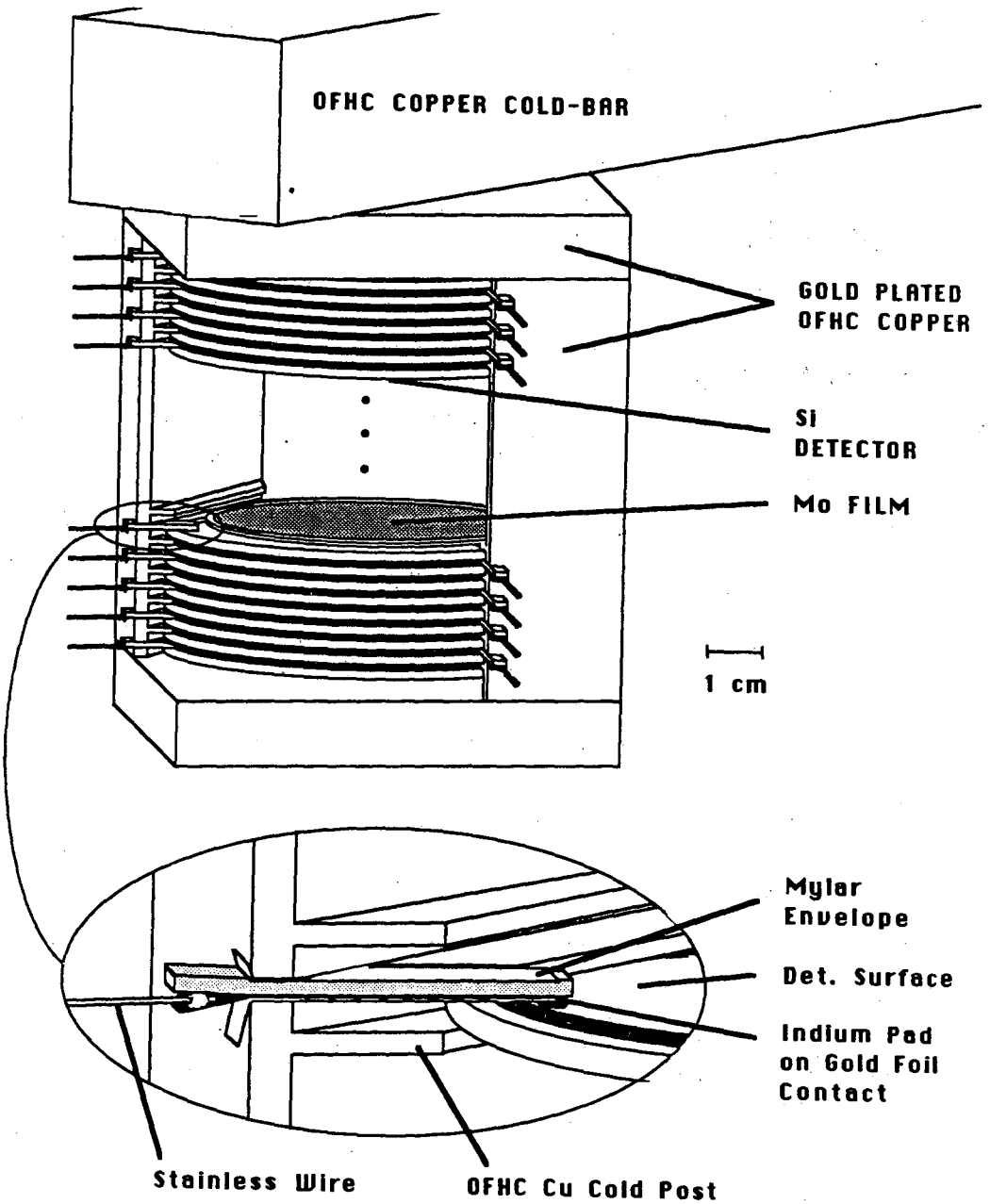

Figure 3.1: **Si detector array and support structure.** A number of the 40 Si detectors in the middle of the array are not shown. The inset shows a expanded view of the region around the electrical contact.

and multiple Compton scattering of gamma rays external to the stack. Double beta decay to the ground state cannot produce a discontiguous event topology. For contiguous two-detector events, backgrounds can be reduced by demanding that the ratio of the energies be within a certain range. For events with energy in three or more detectors, requiring the middle detectors to contain more than the minimum ionization energy of an electron traversing the detector at normal incidence, also eliminates some backgrounds. All of these considerations improve the sensitivity of this experiment to neutrinoless double beta decay. But before going on into more detail, it will be necessary to discuss the apparatus and the online data collection system.

3.1 Si Detectors

The Si detectors used in this experiment were fabricated at the Lawrence Berkeley Laboratory by the Instrument Science and Engineering Division. They are lithium drifted surface barrier detectors. P-type Si is lithium compensated (Li is an interstitial n-type donor) [30]. This effectively produces a very high purity but slightly p-type semiconductor. An n-type guard ring is formed on the top side of the detector by an additional lithiation around the perimeter of the active region of the device. The junction is produced across this surface by applying a thin aluminum coating (20 mg/cm^2), the aluminum acting as an N^+ contact. Gold is applied to the reverse side, forming a P^+ contact (40 mg/cm^2). The detectors must be operated at low temperatures, typically 120° K, to reduce noise associated with

a detector's reverse current. When these devices are fully depleted the dead layers are negligible, being equal to the aluminum and gold thicknesses respectively.

A positive voltage is applied to the aluminum surface in order to deplete the detector. At voltages greater than the depletion voltage, there are no free charge carriers within the semiconductor. An energetic charged particle traversing the Si will ionize electrons, producing electron hole pairs. In Si an average energy loss of 3.6 eV is required to liberate an electron hole pair. The electrons are moved to the aluminum surface and the holes to the gold surface by the internal electric field. The total charge collected on either surface is proportional to the energy lost in the Si. There is no charge multiplication.

At the depletion voltage, the electric field inside the Si detector rises linearly from zero, at the gold surface, to its maximum value, at the aluminum surface. (This field is similar to that of a parallel plate capacitor with a uniform charge distribution between the plates.) In order to get full charge collection from the entire active volume, including near the gold surface, there must be a non-zero electric field everywhere within the volume. This makes it necessary to increase the bias voltage beyond the depletion value. An additional uniform electric field, proportional to the difference between the bias voltage and the depletion voltage, is then formed inside the detector. The above description of the field assumes a uniformly doped semiconductor. Even if this is not the case, it is still in general true that at the depletion voltage the electric field vanishes at one of the detector surfaces. Voltages beyond this value are required in order to get full charge collection.

The array of detectors can be divided into two groups. One group with a depletion voltage of around 40 volts and the other with depletion voltages of up to 60 volts. These groups are biased by separate power supplies, currently running at 64 and 80 volts respectively. There is still however a problem with full charge collection from alpha particles, due to the high ionization density. Higher field strengths are required in this case to break up the electron hole pairs before recombination can occur.

3.2 Mo Films

The Mo films were made by our collaborators at the University of New Mexico. The Mo, which comes in the form of a fine metallic powder, is mixed with formvar, chloroform and cyclohexanone. The resultant slurry is poured into a mold and allowed to dry. By controlling the amount of slurry poured, thickness variations of less than 10% are routinely achieved. Typical films, currently being used for the experiment, are 34 mg/cm^2 thick. A distinct advantage of this technique is that the Mo can be reclaimed and used again in new films of different specifications.

When cooled to low temperatures (120° K) the films tend to curl. To keep them flat and avoid electrical shorts, each film is constrained by a nylon mesh supported by a nylon ring (figure 3.2). This technique allows for the differential expansion between the Mo and nylon supports.

The Mo films are fabricated from an isotopically enriched sample of 1.3 moles. The sample is 98% ^{100}Mo on loan from Oak Ridge National Laboratory. Before

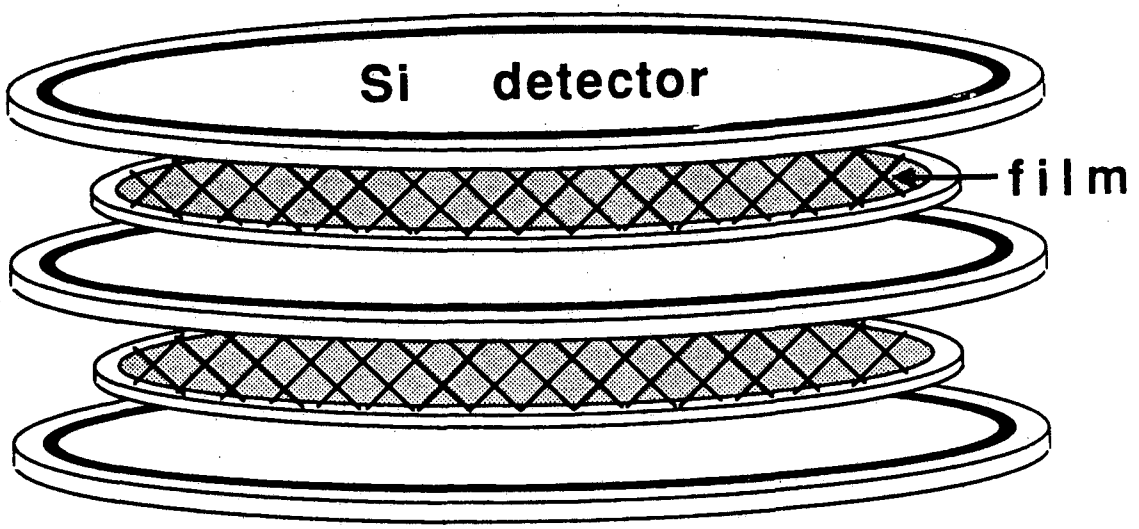

Figure 3.2: **Exploded view of three Si detectors with Mo films.** The nylon mesh and ring is clearly visible.

receiving the sample a small amount (1 gram) was neutron activated to look for radioactive contamination, specifically ^{238}U and ^{232}Th. The sample showed a contamination of 3.2 ± 1 and 6 ± 3 ppb by weight for ^{238}U and ^{232}Th, respectively. Decays from both chains can mimic neutrinoless double beta decay and should be noticeable at this level of contamination. A previous Mo sample, also from Oak Ridge, had much higher levels of contamination. More will be said about contamination later.

There are currently 36 films in the Si detector array. They reside between detectors 3 and 39, one on top of each detector excluding detector 39. The detectors are numbered 1 to 40 from bottom to top. The mass of ^{100}Mo used is 28 grams. Only 21 films were used earlier in the experiment. They were placed between detectors 18 and 39.

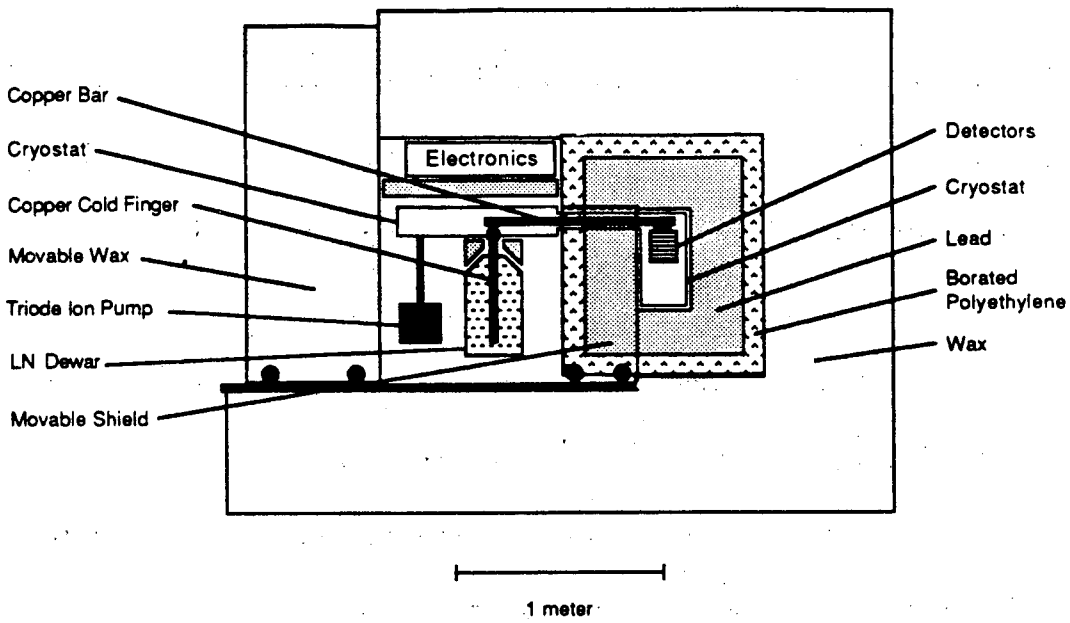

Figure 3.3: **Schematic of the apparatus and shielding**. Shielding thicknesses are: 10 in. of lead, 2 to 4 in. of borated polyethylene and 2 feet of wax.

3.3 Mechanical Apparatus and Shielding

The Si detectors fit into slots, one above the other, in an oxygen free high conductivity (OFHC) copper cage. The cage is suspended from a 1 inch^2 copper bar inside a Ti cryostat (figure 3.1 and 3.3). The detectors must be kept cold (120° K) to function properly. This is done by immersing the other end of the copper bar into liquid nitrogen. The cryostat is evacuated to a pressure of 8×10^{-7} torr by an ion pump, to avoid convective heat flow (a sorption pump is used first as a clean roughing pump to reach a pressure of $1 - 10 \times 10^{-3}$ torr). In addition, the detectors are surrounded by a cold 5 mil gold shield (not shown in figure 3.1) to reflect infrared radiation from the cryostat walls. Most of the copper bar and all

of the copper cage is gold plated.

The cooling system uses an average of 7 liters of liquid nitrogen a day. The dewar used to cool the copper cold bar can only hold 30 liters. Since the system may be left unattended for as long as a week, a 50 liter pressurized supply dewar is used to automatically fill the smaller dewar. Sensors inside the 30 liter cooling dewar control the fill. Filling cannot occur, however, without permission from the data collection program. This is done to avoid collecting spurious events caused by microphonics generated during the liquid nitrogen transfer. The process is coordinated by a custom designed controller box.

Electrical contact is made to the top surface (aluminum side) of the detector via a narrow gold strip (see inset in figure 3.1). The gold is insulated by a mylar envelope. The mylar also serves to wedge the gold firmly against the aluminum surface. A small amount of indium, at the gold aluminum interface, makes the electrical contact. The gold strip is connected on its other end to an insulated wire, which in turn connects to BNC vacuum feedthrough near the back of the cryostat. To minimize heat flow, the gold is connected to the insulated wire through thin .5 inch long piece of stainless steel wire. The bottom surface (gold side) of each detector is grounded to the copper cage which, along with the rest of the cryostat, is the main ground for the system.

There are two cable ways, inside the cryostat, on either side of the copper cold bar to carry the signal lines. Lines from odd numbered detectors use one cable way and even numbered detectors use the other. This reduces crosstalk between adjacent channels to near zero. The signal lines have no ground shields. This was

done to minimize possible sources of radioactivity and the capacitance to ground seen at the input of the electronics. With our electronics, the crosstalk introduced by the lack of shielding is less than .3% relative to the signal amplitude, for two adjacent lines.

Radioactivity is a major concern in an experiment of this type. All materials used in its construction were selected for their low levels of contamination. A special low activity germanium detector, fabricated by Canberra, was used to count samples. The germanium detector was surrounded by a low activity lead shield and an active cosmic ray veto. The lead covered all sides and the scintillator veto surrounded the lead on five sides, excluding the bottom. With this setup, contaminations of 1-25 ppb by weight, for ^{238}U and ^{232}Th, could be detected depending on counting time and sample size and geometry. All materials used in the construction of the experiment, which are not shielded from the detector stack, showed no measurable contamination.

The detector stack is shielded by 10 inches of low activity lead, surrounded by 2 to 4 inches of 5% borated polyethylene and 22 inches of wax (figure 3.3). Most of the cryostat and all of the electronics and cooling system is shielded from the Si detector stack by a 10 inch lead door. The cryostat penetrates the door through a 2×4 inch aperture and moves along with the door on steel rails when access to the interior cavity is required. The cooling dewar and electronic are also mounted behind the door and move with it. When it is closed, the door fits snugly into the lead shielding leaving no straight line cracks to the outside. Mounted on the same set of rails behind the cryostat is a wax door. It completes the neutron shielding.

The entire shield provides a calculated factor of 10^4 and 10^5 reduction in external neutron and gamma ray background at 3 MeV, respectively.

3.4 Experimental Site

The experiment is located 3950 ft. underground in the Consolidated Silver Mine in Osburn, Idaho. The cosmic ray intensity at this depth (3290 meters of water equivalent) has been measured to be $.44 \pm .13 \frac{counts}{cm^2\, sr\, year}$. The measurement was done using four 1×2 ft. $\times 1$ inch thick scintillators in coincidence (2 counts/day in this detector). Rock samples taken from the experimental area were found to contain 3.3% K, 10.7 ppm Th and 4.0 ppm U, by weight. Radon daughter activity in the air was measured at 6 picocuries per liter.

By far the most troublesome background has been caused by radon. In April of 1987 the ventilation pattern in the mine was changed, exposing the experiment to radon contaminated mine air. The raw event collection rate in our system doubled. To counter this problem, the air flow was modified. In addition, an inflatable mylar gasket was installed around the lead door in the experiment's shielding. When the door is closed and the gasket pressurized, air flow into the cavity containing the Si detector stack is severely restricted. The cavity itself is continually flushed by clean nitrogen gas, obtained by boiling liquid nitrogen. These modifications reduced the data collection rate by a factor of 6. A factor of 3 gain over the original data collection rate. The experiment uses 12 liters of liquid nitrogen a day for this purpose. This corresponds a flow of 5.3 liters/minute of

nitrogen gas at STP.

3.5 Electronics

Voltage is provided to each detector via a bias voltage bus (figure 3.4). The detectors are connected to the bus by an 8 M ohm isolation resistor. In turn, the bus is connected to its power supply via a 750 K ohm resistor. A .1μf capacitor from the bus to ground acts along with the 750 K ohm resistor as a low pass filter, eliminating ac ripple from the power supply. There are two bias voltage power supplies, labeled HV1 and HV2. HV1 powers detectors 1-20, excluding detector 9 and 12. HV2 powers detectors 21-40 and detectors 9 and 12. As mentioned before, the detectors on HV1 have depletion voltages of around 40 volts, while those on HV2 are as high as 60 volts. In general the detectors on HV1 have lower breakdown voltages than the detectors on HV2. Preamps are connected to each detector via a .1μf bias voltage blocking capacitor. The bias voltage bus along with other circuitry is inside an electronics box, on the outer side of the lead shielding (figure 3.3).

When fully depleted each detector has a capacity to ground of 270 pf. The signal lines connecting the detectors to the electronics are about 6 ft. long, 4 ft. of unshielded insulated wire inside the cryostat and another 2 ft. of shielded cable outside the cryostat. This adds approximately an additional 120 pf. The capacitive load on the preamplifier input is then 390 pf to ground.

It is the purpose of the electronics to measure accurately the number of free

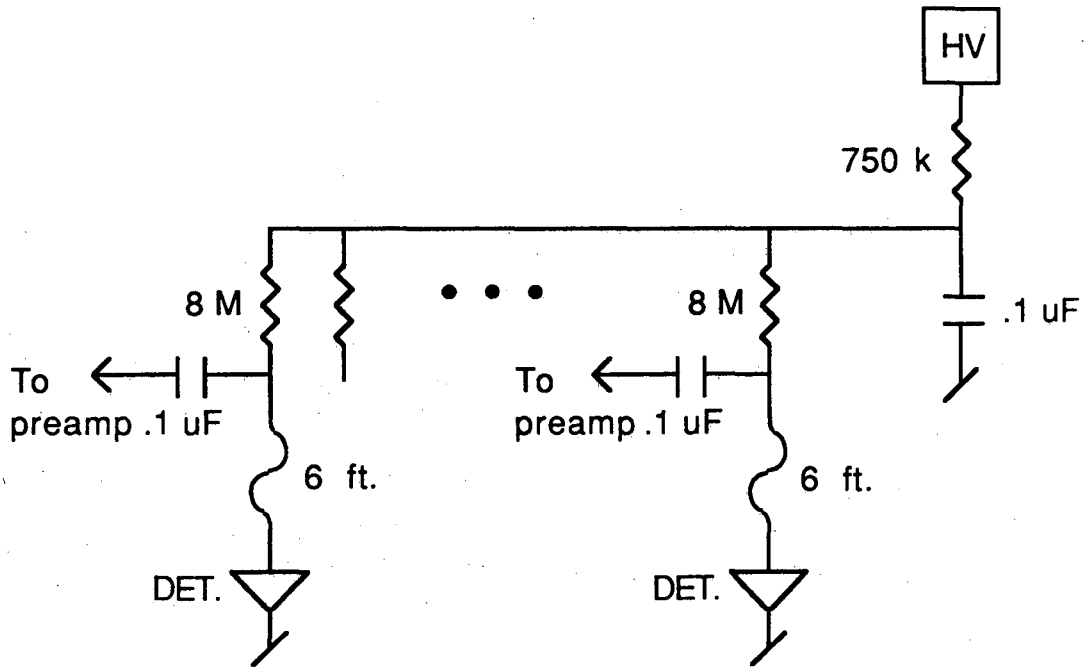

Figure 3.4: **The bias voltage bus** with associated circuit elements.

charge carriers produced in each detector and thus the deposited energy. To do this the charge is collected from the detector by a charge sensitive preamplifier. Charge sensitive preamplifiers collect almost all of the charge off the detector because of their high open loop gain A. The preamp can be represented by an effective capacity to ground of AC_f, where C_f is the preamp's feedback capacitance. Charge generated in the detector splits between the detector, the signal line and the preamp in proportion to their capacitances to ground. The large gain A also explains why the crosstalk between channels using the same cable way inside the cryostat is so small. Crosstalk occurs between channels i and j because of the stray capacitive coupling C_{ij} between wires. It can be shown that this coupling can be treated as another capacity to ground. The relative size of the charge induced on channel i due to a signal on channel j is then $\frac{C_{ij}}{A_j C_{fj}}$, a small number.

The charge sensitive preamplifiers used in this experiment were manufactured by Micron Semiconductor, Ltd. of Sussex, England. For this device C_f equals 2 pf and the feedback resistance, R_f, equals 100 M ohm. The preamp output decays exponentially with a decay time of 200 μsec. With 390 pf to ground at the preamp input, the rise time is about 75 nsec. The conversion gain is 22 mvolt/MeV. The output is capacitively coupled to all other circuits.

The preamp output goes to the relatively slow shaper circuit (figure 3.5). This circuit produces an output pulse with very good signal to noise ratio and is used for a precision determination of the energy. The shaper consists of a differentiation stage followed by two integration stages. The differentiation, at the input of the circuit is pole zero adjusted to compensate for the 200 μsec falltime of the preamp.

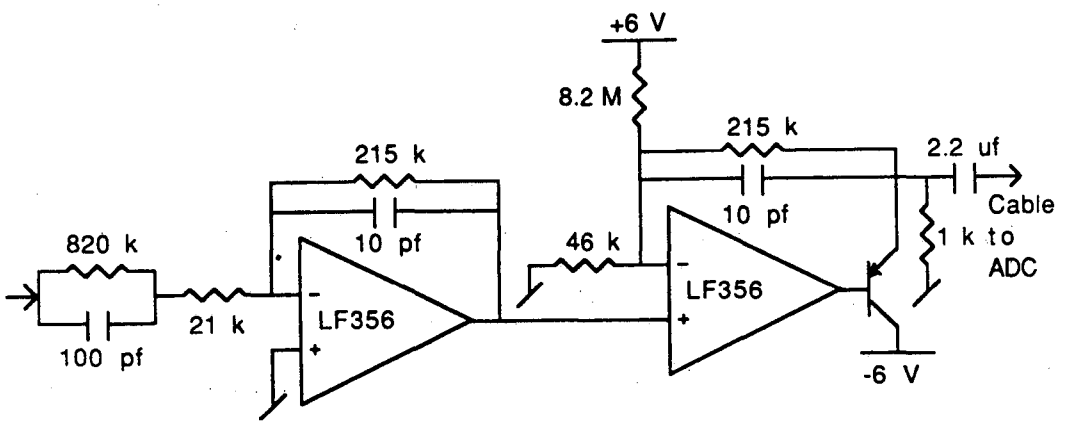

Figure 3.5: **Shaper amplifier circuit.** The first *RC* combination (from the left) with a 2.15 μsec time constant, combination acts as a differentiation stage. The other *RC* pairs with this time constant are integration stages.

The integration stages are in feedback positions on the operational amplifier. All *RC* constants are 2.15 μsec, producing a unipolar output pulse of risetime 4.0 μsec. The resistor connected to the +6 volt supply on the second stage is used to set a DC output pedestal and the transistor in the feedback provides enough current on output to drive 50 ohms.

With identical *RC* constants in each stage, the gain of the circuit depends only the ratio of resistors and should be insensitive to thermal fluctuations. Although all differentiation and integration RC constants are identical, the individual values of resistors and capacitors are not. This allows the circuit to provide gain as well as shaping. The circuit is quite linear with an output peak value of around 250 mvolt/MeV. There is a 10% variation from channel to channel.

A peak sensing ADC, LeCroy CAMAC Model 2259B, is used to digitize the

pulse height. Each module has 12 input channels with 11 bit voltage resolution. The input voltage pulse must have an amplitude between 0 and −2.0 volts. The ADC inputs have a built in 50 ohm termination to ground.

Because of problems with microphonics, the shaper output is no longer dc coupled to the ADC as originally planned. Instead, the coupling is through a 2.2 μf capacitor (figure 3.5). The capacitor together with the 50 ohm termination resistor in the ADC, act as a highpass filter with a 110 μsec RC constant. This attenuates the microphonics, which have a dominant frequency of about 1 kHz, without severly affecting the shaper output.

Overall energy resolution (FWHM) for an individual detector channel ranges from 10 - 21 keV, as measured using a gamma ray source. The average resolution is 14 keV. This compares well with the preamplifier specifications. The preamp is characterized by a noise slope of 15 eV/pf and an intercept of 5 keV, when used with a Si detector. With 390 pf on the input, the FWHM should be 11 keV.

The low noise slope is a consequence of the high transconductance of the FET (2SK 147) used in the preamp. There is a trade off however. FETs with a large transconductance also have large intrinsic capacitance. This capacitance when multiplied by the noise slope accounts for most of the 5 keV noise intercept. While appropriate for systems with large detector capacitance such as ours, the large noise intercept would not be suitable for low capacitance detectors. FETs with smaller transconductance and hence smaller noise intercept are preferred in this case.

Another possible source of noise is shot noise. Shot noise is associated with

the discrete nature of the charge of the electron e and the reverse current I_R in a detector. An approximate formula for this effect, given our shaper circuit, is

$$4.46\sqrt{\frac{I_R\tau}{e}}\ eV$$

Where τ is the 2.15 μsec RC constant of the shaper circuit. Typical reverse currents in a detector are about 10 nanoamps. This implies a negligible contribution of 1.6 keV to the FWHM due to shot noise. (the gaussian line shape of the gamma ray peak, see calibration section, implies that the FWHM values should be added in quadrature)

Microphonics present a problem in this experiment. It accounts for the additional noise. Specifically, detectors with an anomalously large FWHM are known to be more microphonic. The 1 kHz sine wave generated by microphonics on these channels can be 2-3 times the size of the white noise band as seen on an oscilloscope. It is suspected that the copper cage holding the detectors acts as pendulum, coupling to the torsional modes of oscillation of the copper bar it is suspended from. This feeds into the electrical system via the stray capacity to ground at detector contacts. So far it has not been possible to damp the mechanical oscillation directly.

The preamp output also goes to a relatively fast timing circuit (figure 3.6). This circuit produces an output pulse height proportional to the energy input, but with a poorer signal to noise ratio because of its short time duration. The circuit is essentially a linear amplifier followed by a single differentiation, with a short time constant. This produces a unipolar output with risetime of around 100 nsec and

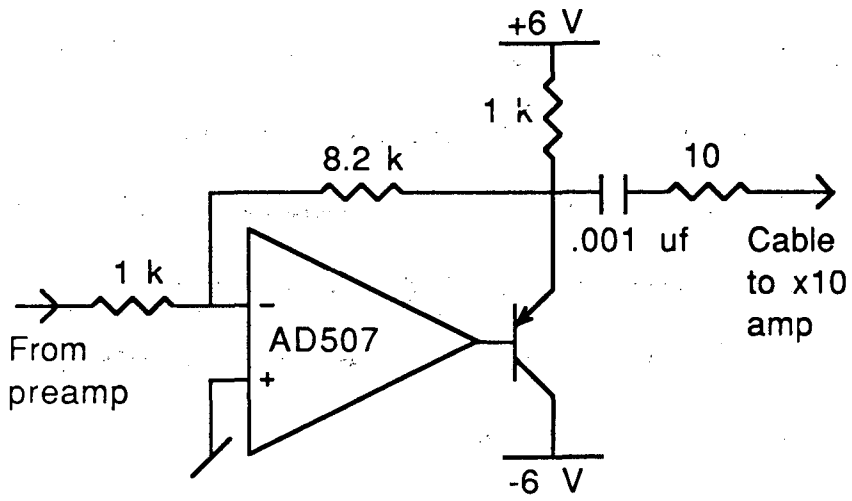

Figure 3.6: **Timing and triggering circuit.** The .001 μf capacitor along with the effective 60 ohms of resistance (50 ohm cable and termination) on the output differentiate the signal with a 60 nsec time constant.

with a comparable falltime. The design here is a compromise between signal to noise and pulse width, since the output is both used as a system trigger and for detection of multiple events with short temporal separation. The conversion gain is approximately 65 mvolt/MeV.

The logic involved in the trigger and the connections for the signal output are summarized in upper left part of figure 3.7. The output of the timing circuit drives a linear amplifier which provides a factor of 10 gain before the pulse is discriminated to produce an event trigger. Discriminator levels are currently set at 300–450 keV. Output pulse widths are at 100 nsec. These NIM level logic pulses are added together and sent to a gate generator, which gates the ADC modules with a 2 μsec pulse, initiating an event read. The gate is generated 3 μsec after

the initial trigger pulse, in coincidence with the peak of the shaper output.

The sum of the 100 nsec discriminator output is also used to start and stop a 100 MHz clock. A custom built controller box generates an inhibit signal for a CAMAC scaler. The scaler counts the input pulses from a 100 MHz oscillator only when the inhibit is removed. The scaler is reset to zero by a CAMAC crate clear signal, which is sent at the start of a run and at the end of every event read. A timing pulse above discriminator levels will remove the inhibit, starting the scaler and initiating an event read. A second pulse during the read will reset the inhibit signal, stopping the scaler. At the end of the read before the CAMAC clear signal is issued, the scaler is examined to see if it has stopped. If so, the time between the two trigger pulses is recorded with the event. This "fast clock" provides information on relatively shorts lifetimes in decay chains, e.g. ^{212}Bi followed by ^{212}Po in the the thorium chain. The upper right of figure 3.7 summarizes the logical connections involved in the operation of the "fast" and "slow" clocks.

3.6 System Safety Features

Since the experiment may be unattended for as long as a week, a number of safety features have been incorporated into the system. They are designed to protect the detectors and data from damage due to power failure, loss of vacuum and malfunction of the automatic liquid nitrogen filling system.

An uninteruptable power supply (UPS) is used to provide power line conditioning and battery backup in case of power failure. The batteries will last 1 hour

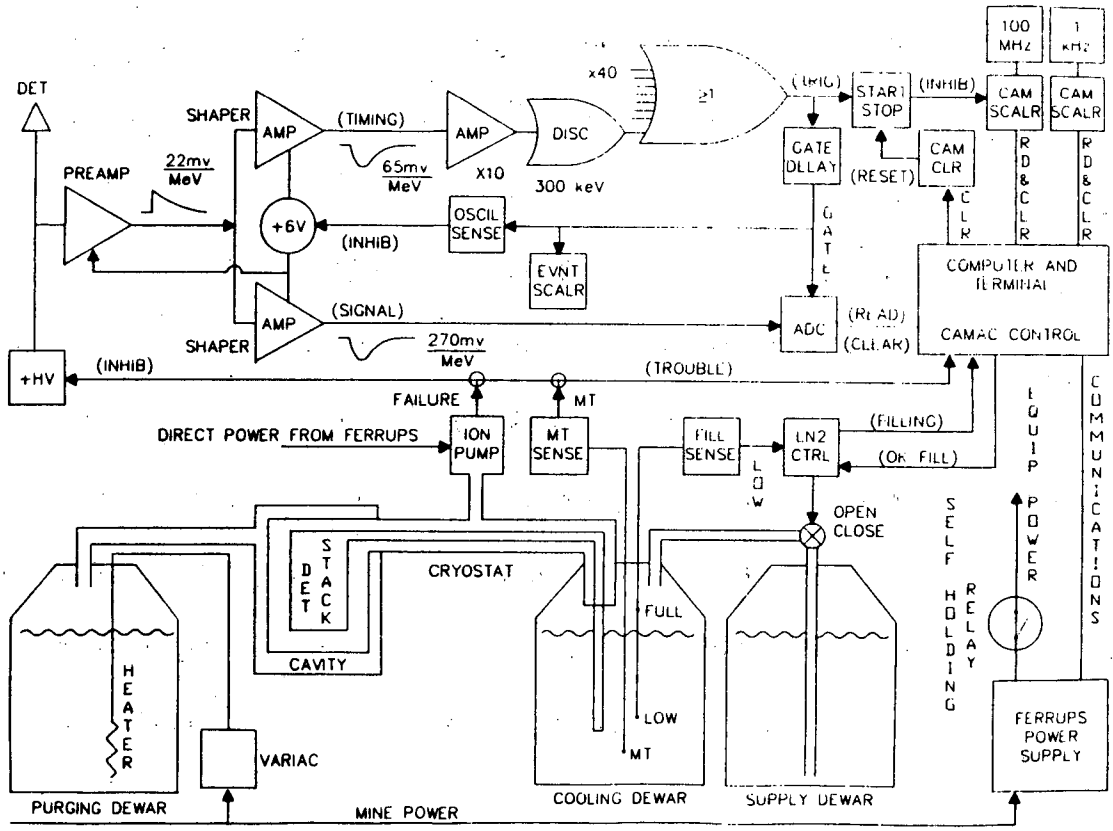

Figure 3.7: **Schematic of electronics and control system.** The electronics and trigger logic are in the upper left of the diagram. Logic for the fast and slow clock are in the upper right. The control systems and safety features are in the lower half of the diagram.

before shutting down at current power loads. Except for the ion pump, all power to the experiment is supplied from the UPS through a self holding ac relay. The relay must be manually reset to return power to the system after battery shutdown. This stops the system from powering up after battery shutdown and the return of line power. The ion pump has a built in protection circuit and is powered directly from the UPS.

The computer communicates with the UPS through an RS-232 interface. The date, time, battery voltage and inverter status are read from the UPS. The inverter will be on only if the system is running on batteries during a power outage. Under normal operation the batteries are charged to 52 volts. In the event of a power failure, the UPS will provide power until the battery voltage drops to 41 volts. In order to protect the data already accumulated, data collection is stopped and all files are closed when the inverter is on and the battery voltage drops below 44 volts.

Both high voltage supplies have an inhibit input on the back panel. This input sets the output voltage to zero when grounded. The inhibits are connected to both the ion pump and a liquid nitrogen level sensor inside the cooling dewar though ac relays. If either the ion pump fails or liquid nitrogen level falls below the height of the sensor, the relay grounds the inhibit, resetting the detector voltages to zero. This level sensor is not the same as the one used to fill the 30 liter cooling dewar. It is set 5 liters below the filling sensor. It is used as a safety, to turn off the bias voltage, if the filling system malfunctions.

Relays are also used to inform the computer of a high voltage shutdown. An

ADC input is connected through a 1 K ohm resistor to minus 6 volts. The ADC input is also connected to ground via two relays. The relays are in series and are normally closed. The ADC then measures zero volts when read. In case of ion pump or liquid nitrogen fill failure, the ground connection is broken and the minus 6 volts divides between the 1 K ohm and the 50 ohm internal resistance of the ADC. The ADC then reads minus 286 mvolts, causing the computer to terminate data collection and close all open files.

The timing circuit is prone to 1 MHz oscillations. The system is rendered useless when this occurs, saturating the trigger system and generating spurious forty-detector events. The oscillations seem to be triggered by spikes in the voltage lines powering the electronics. To counter this problem, a number of *RC* filters have been added to the system. While mitigating the difficulty, this has not solved it. The oscillations can be stopped, once started, by cycling the +6 volt power to the timing circuit on and off. This is now done automatically. A monitoring circuit samples the trigger rate. If the rate exceeds 10 Hz (the data rate is only 1 event/minute), the AC power to the +6 volt power supply is turned off and on via a relay. This stops the oscillation. A signal is also sent to a CAMAC scaler to count the number of times during a data run that the switch has tripped. The dead time caused by the power switching is less than 3 minutes in a 90 hour run, about .06%.

The bottom half of figure 3.7 summarizes the safety and control features of the experiment. The UPS is referred to by its trade name (FERRUPS) in this diagram.

3.7 Data Acquisition

Data is collected using CAMAC modules and a Kinetics Systems microcomputer and CAMAC crate controller. A gate pulse into any of the five ADC modules in the CAMAC crate generates a Look At Me (LAM) signal, starting the event processing. All forty detector channels are read and compared against individually set software discriminators. These are not the same as the hardware discriminators used on the timing circuit to generate the ADC gate. The software discriminators vary from 80 to 110 keV. Only detectors with pulse heights above their software discriminator levels are kept as part of the event record.

The event record also contains the "fast" and "slow clocks". The slow clock simply records the time between events in milliseconds. To be more precise, a 1 kHz pulse generator is counted by a CAMAC scaler. The scaler is read and cleared at the end of every event read. The time interval is measured from the end of processing of the previous event to the end of processing of the current event. The "fast clock" is described in an earlier section. It measures the time from the beginning of the event to any subsequent event which may occur during the processing.

The size of an event record depends on the number of detectors in the event. The computer uses 16 bit words to store integer variables. For each detector that fires (above software discriminator) two words are required, one for the detector number and one for its pulse height (pulse heights are 11 bits long, 0 to 2047 decimal). The "fast" and "slow" clock both require two words each. An extra

word is used to store the length of the event (in words). An event firing one detector requires 7 words; two detector, 9 words and so on. The event records are stored in a 512 word block of computer memory. When the block is full it is written into a data file on a floppy disk. Only one out of five events fires more than one detector. As a result, each data block holds approximately 67 events. At the current event rate of 1 event/minute, a block is written to disk approximately once every hour.

There are two eight inch floppy disk drives connected to the microcomputer. One drive is used by the systems disk which stores the operating system and data collection routines. The disk in the other drive is used for data collection.

A data file stores the event records from the data run. There are two additional records in this file. The "begin run" record stores the experiment and run numbers, the starting date and starting time. The "end run" record records the total number of events in the run, the live time, ending date and time, and the number of times the +6 volt power supply has been cycled off and on (see section 3.6).

A second file, the "run log", contains a brief summary of the run. The time and date when each block of data was written to disk is listed along with the time and duration of each liquid nitrogen transfer to the 30 liter cooling dewar. A list of new and old (used for the last run) software discriminators appears at the beginning of the "run log". At the start of every run, software discriminators are checked against measurements of zero energy pedestals. If significant changes have occurred new software discriminators are set. In most cases no changes occur.

Every 10 minutes, data collection is disabled and a number of system safety

checks are made. It is at this time that the computer interrogates the UPS and the ADC monitoring the bias voltage inhibit. All detector ADCs are checked by sending in a gate pulse to monitor pedestal levels. When read, a zero-detector event is expected. If more than two detectors are above their software discriminator levels, the zero energy pedestals are remeasured and new software discriminators are set. The new settings are written to the "run log". In addition, the electronics are tested by simultaneously sending a test pulse, equivalent to 1 MeV, to all 40 channels. The system expects to see a forty-detector event as a consequence. An error message is written to the "run log" if this does not occur. Power failure and bias voltage shutoff also generate messages in the "run log".

3.8 Calibration

A Digital to Analog Converter (DAC), along with precision pulse generator, calibrates the electronics. The DAC operates in the CAMAC crate under computer control. It has eight outputs which can be individually set to any dc level between ± 10 volts. Two of these outputs are used to control the precision pulse generator. The first output provides a dc reference level to control the height of the generated pulse. The second output triggers the pulse generator when switched on and off between between 0 and 5 volts. An additional DAC output goes directly to the gate and delay generator. This allows the ADCs to be gated without a trigger from the timing circuit. Zero energy pedestals are measured in this way.

Before each data run the electronics is calibrated. A series of 40 test pulses at

each of 20 pulse heights is sent from the precision pulse generator into the front end of all preamplifiers through a built in 2 pf test capacitor. The test pulses have risetimes of 50 nsec and falltimes of 200 μsec. The charge generated on the test capacitor by the 20 pulse heights simulate events with energies of 0 to 7.6 MeV inclusive, in increments of .4 MeV. This covers the full range of the ADCs (0-2047).

Electronic calibrations are collected on a separate floppy disk and mailed along with the previous data run to Berkeley for analysis. The 40 pulses at each pulse height are well fit by a gaussian distribution. The means and sigmas of the fits generate calibrations for each channel. The calibrations take the form

$$PH = A + BQ + C\exp(-DQ) \tag{3.1}$$

where PH is the pulse height, in counts (0-2047), measured by the ADC; Q is the energy measured in MeV; and A, B, C and D are constants differing from channel to channel. Typically, the exponential is negligible above an energy of 1.2 MeV. In this region the calibration is linear with B approximately 250 counts/MeV. Sample values for all coefficients are given below.

The energy Q is only known to 10% accuracy because of variations in the value of the 2 pf test capacitors. To calibrate the system precisely a ^{228}Th source is used. Only single-detector events are collected. The spectrum obtained for each channel contains only one peak above the hardware discriminator level, the double escape peak. This peak is generated by the pair production of the 2.615 MeV gamma ray emitted in the decay of ^{208}Tl at the end of the Th chain. Both annihilation

gamma rays escape producing a peak at 1.593 MeV. The peak is fitted by a gaussian distribution, with an average width of 14 keV (FWHM). The centroid of the gaussian along with an electronics calibration, taken just before or after the Th source calibration, defines a scaling factor S, which effectively calibrates the test capacitor.

$$E = SQ$$

where E is the actual energy deposited in the detector and Q is the energy as measured by the electronics calibration. The factors A, B, C, D and S define the calibration for each channel. Sample values are -21, 253/MeV, 52, 3.3/MeV and 1.09, respectively.

Other gamma rays in the Th chain do not readily produce peaks, because they are not energetic enough. The photoproduction cross section is negligible above 400 keV in Si and Compton scattering does not generate peaks in the spectrum. Only gamma rays with a significant pair production cross sections can produce this feature in detectors of our size. Pair production increases rapidly with photon energy above the 1.02 MeV threshold.

Testing of the DAC and precision pulse generator along with the preamplifier and shaper circuit was done at Berkeley before going to the mine site. Using a Pulse Height Analyzer (PHA), the relative accuracy of the shaper output was checked. Centroids of peaks were accurate to 1 keV. Weekly drifts were less than 2 keV, being randomly directed from week to week. The system was found to be quite linear, the non-linearity in equation (3.1) coming from the ADCs. Source

calibrations were also done at Berkeley. The double escape peak from ^{208}Tl, the 238 keV photopeak from ^{212}Pb and a number of Compton edges were used to assess linearity and stability of the precision pulse generator. The above results were confirmed.

At the mine site, the system has not been as stable. The ADCs routinely drift 10 keV at 3 MeV from run to run. On some channels a drift of over 100 keV has been observed. These large drifts are thought to be associated with problems in the detector contacts, rather than in the ADCs.

The electronics calibrations have mapped these drifts accurately. Thorium source calibrations, done once every few months, show relative changes in the scaling factor S of only .2%. This corresponds at 3 MeV to a 6 keV change, well within the 14 keV energy resolution of a single Si detector. However, drifts in the ADCs are comparable to a detector's resolution and uncertainty as to when these drifts occurs during the course of a data run, degrades a detector's performance. Given the expected full width of 340 keV for the neutrinoless double beta decay peak (see section 4.1), these uncertainties in the energy are not a problem.

Chapter 4

Data Analysis

4.1 The Event Signature

For electrons in Si minimum ionization occurs at a kinetic energy of 1 to 1.5 MeV, with an energy loss of 3.6 MeV/cm. At normal incidence with no scattering, a minimum ionizing electron will lose .5 MeV in a .14 cm thick Si detector. This implies that for the neutrinoless double beta decay of ^{100}Mo with two electrons sharing 3 MeV of energy, a decay event will deposit energy in no more than six detectors. Detailed Monte Carlo calculations verify this conclusion (see section 4.2 for details of this program), although the assumption of no scattering is far from accurate. Figure 4.1 shows a typical trajectory from the Monte Carlo simulation. The spatial extent of the event is clearly limited by scattering. This event deposits energy only in two Si detectors. As it happens this is the most likely situation. Figure 4.2 shows the number of events in a 1000 event Monte Carlo simulation which deposit energy in one or more detectors. Most of the events are contained

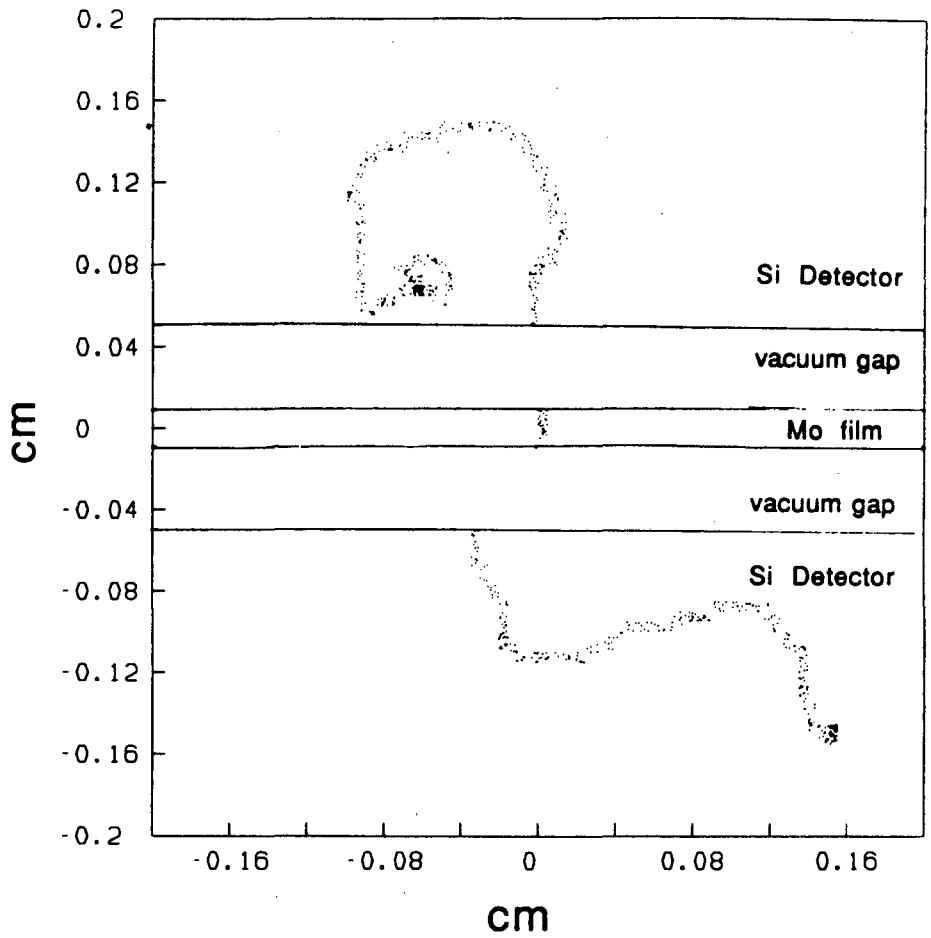

Figure 4.1: **Monte Carlo Simulation** of a neutrinoless double beta decay event. The figure is a projection of the trajectories of a single event onto the X, Z plane where Z (vertical axis in figure) is the symmetry axis of the detector array. The dot density is proportional to the local energy loss.

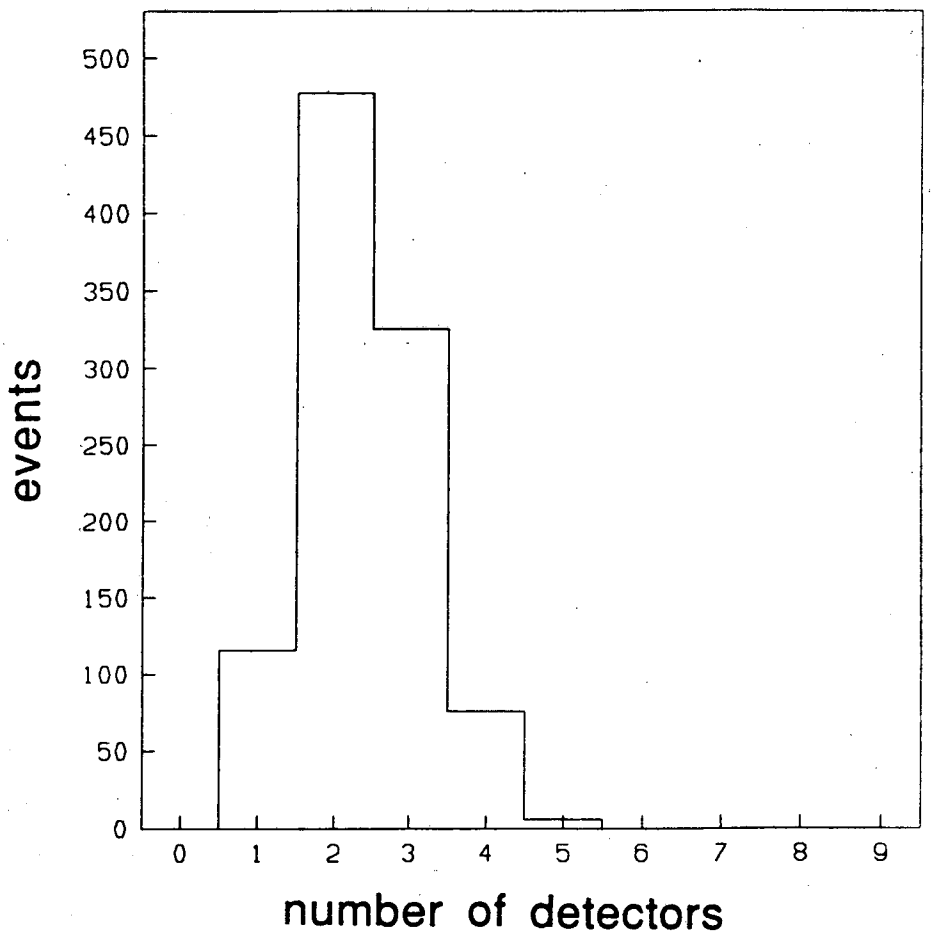

Figure 4.2: **Number of events versus number of detectors containing energy**, from a 1000 event Monte Carlo simulation of neutrinoless double beta decay.

in two or three detectors. There is only about a 10% chance of an event depositing energy in only one detector. As will be seen later in this chapter, for energies above 2 MeV, the actual data events consist mostly of one-detector events. These are alpha particles which have lost some of their energy in traversing dead material before entering the sensitive region of a Si detector. Removal of these events reduces the background by almost two orders of magnitude with only a minimal reduction in the efficiency for collecting neutrinoless double beta decay events.

The above estimate would seem to indicate that a minimum of .5 MeV of energy would be deposited by an electron in traversing a single Si detector. This is not quite correct because of energy straggling. The 3.6 MeV/cm value used above is the average energy loss for minimum ionizing electrons. The most probable energy loss is slightly lower and fluctuations can make the minimum energy deposit lower still. Density effect corrections also reduce the stopping power. Figure 4.3 shows results of the Monte Carlo simulation. The number of events versus energy deposited in middle detectors, for events with energy in three or more detectors is histogramed. The peak of this distribution occurs at 525 keV and the midpoint of the sharp rise on the low energy side is at 450 keV. There are only two events below 400 keV. This feature is useful in rejecting backgrounds. Multiple Compton scattering of gamma rays and beta-gamma or alpha-gamma cascades can produce contiguous multi-detector events. If one or more of the middle detectors in an event contain less than 450 keV of energy, the event can be rejected without seriously affecting the double beta decay collection efficiency.

For events which deposit energy in two detectors, a useful parameter is the

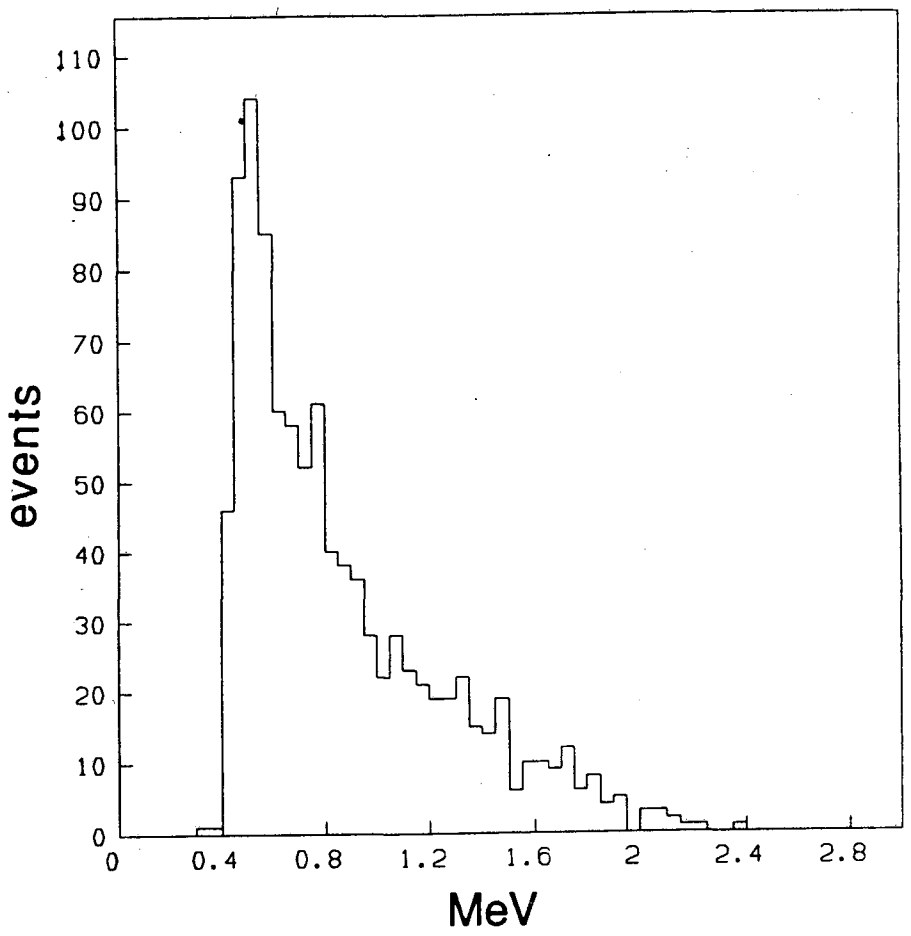

Figure 4.3: **Number of events versus energy deposited in the middle detector**, for event which deposit energy in three or more detectors from a Monte Carlo simulation.

ratio of the two energies. Figure 4.4 shows the distribution obtained from the Monte Carlo simulation. The zero in the first bin (0.–.04) is enforced by a set of preliminary cuts which are used on both the actual events and on the Monte Carloed events (see section 4.3). Otherwise no biases have been introduced. This distribution will be compared later to that of the actual data sample to determine whether the events are consistent with double beta decay.

Finally, in figure 4.5, the Monte Carlo result for the spectrum of total event energies is shown. The fitted lineshape has the functional form,

$$x^{1.98}e^{-x}; \quad x = (3.033 - E)/.102 \quad x \geq 0$$

where E is the total energy in MeV. The peak occurs at 2.8 MeV. The full width (FWHM) is approximately 340 keV and contains 72% of the events. The total energy spectrum would be a delta function at the decay energy of 3.033 MeV if it were not for the energy loss within the Mo films. The films are 85% Mo, 7% O, 7% C, and 1% H by weight. The average density (2.05 gm/cm^3) and thickness (.0165 cm) lead to a thickness in gm/cm^2 of .034.

4.2 Monte Carlo

The Monte Carlo program used to simulate double beta decay is designed to track electrons at energies and in materials where radiative energy losses can be neglected. After choosing a starting position, energy and direction, the program randomly selects a step length which correspond to 100 to 200 scatterings from the nuclei of the material being traversed. This has the virtue of making the multiple

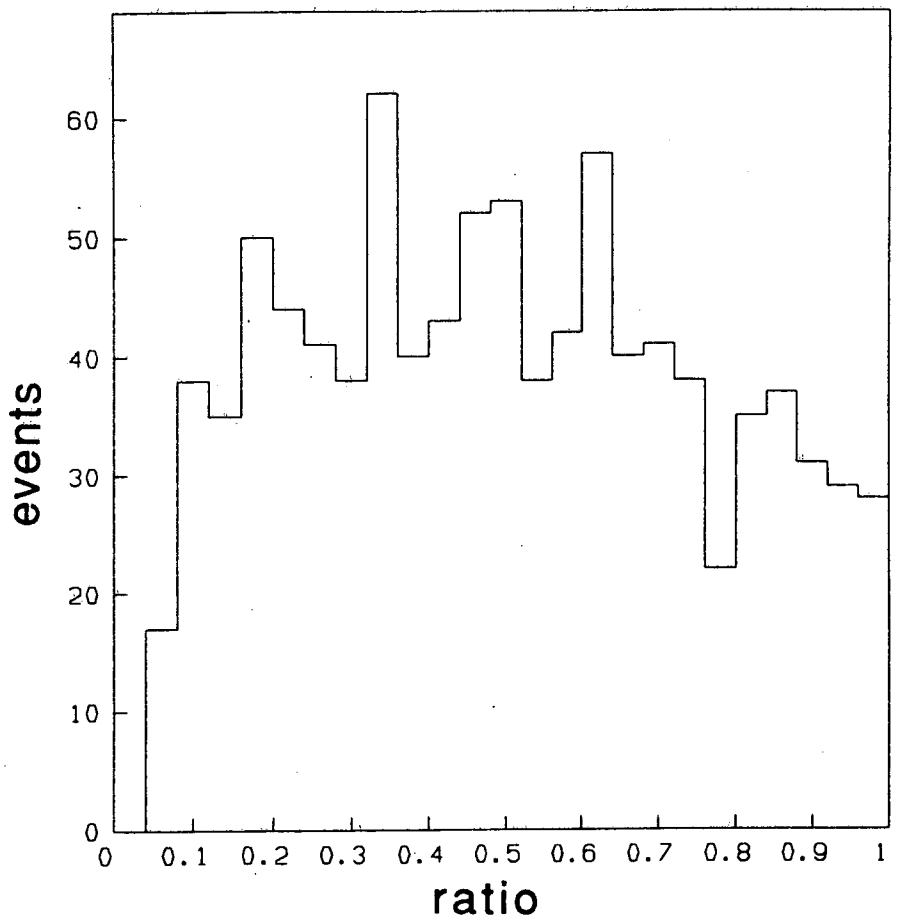

Figure 4.4: **Ratio of the energies** for events which deposit energy in only two detectors from a Monte Carlo simulation. The ratio is restricted to the interval 0.– 1. by dividing the smaller energy by the larger. There are about 1000 events in the figure.

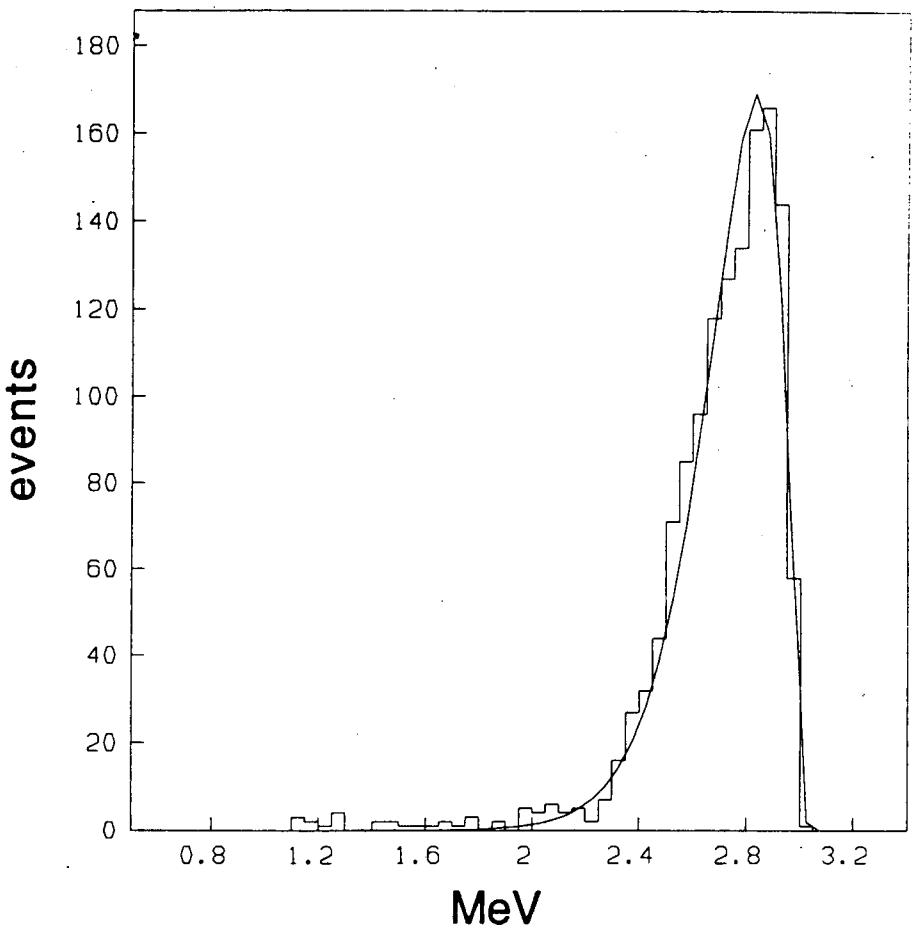

Figure 4.5: **Total energy spectrum** for neutrinoless double beta decay from a Monte Carlo simulation.

scattering distribution approximately gaussian for small angle scattering. This also has the added advantage of making the energy loss distribution only weakly dependent on electron energy. The energy loss per step is Landau distributed [31] over the full range of electron energies considered in double beta decay. After moving the electron a step length and calculating an energy loss and scattering angle for that step, the energy is appropriately decremented and a new direction is calculated. The process then begins over again with the selection of a new step length. This continues until the electron has no energy left. The step length is proportional to β^2 (β is the electron velocity). For both Si and the Mo films the step length is from 16–32 μm at $\beta = 1$, the variation caused by randomly selecting from 100 to 200 scatterings.

The Monte Carlo program selects the initial characteristics of the double beta decay event. The total decay energy of 3.033 MeV is split between the two electrons. An opening angle between the electrons is selected as is an initial starting position for the decay within the Mo film. The decay is assumed to occur randomly within the film. The single electron energies and opening angles are picked according to the single electron spectrum and angular distribution appropriate for the double beta decay mechanism being considered. These mechanisms were discussed in chapter 2. In general the results of the Monte Carlo simulation are insensitive to the differences between mechanisms. Table 4.1 shows the probability of an event depositing energy in N detectors as a function of the decay mechanism. The neutrino mass mechanism generates electrons according to the unimodal single electron spectrum of figure 2.6, with an angular correlation of

decay mechanism	1 det.	2 det.	3 det.	4 det.	5 det.
neutrino mass	.09	.48	.34	.08	.01
RHC vector	.12	.50	.31	.06	.01
RHC scalar	.08	.44	.36	.10	.01
phase space	.11	.48	.32	.08	.01

Table 4.1: **Probability of N detectors containing energy** in a neutrinoless double beta decay event from a Monte Carlo simulation. Accuracies range from .005–.02 for small and large probabilities, respectively. Most differences are not significant. Mechanisms are defined in the text.

$(1 - \beta_1\beta_2\cos(\theta))$. The RHC vector term uses the same one electron spectrum, but has a $(1 + \beta_1\beta_2\cos(\theta))$ angular correlation. The RHC scalar term uses the $(1 + \beta_1\beta_2\cos(\theta))$ angular correlation, but with the bimodal one electron spectrum of figure 2.7. The last line, which is listed as phase space, uses the unimodal single electron spectrum as in the neutrino mass mechanism, but with no angular correlation. All differences are minor and most are within the statistical uncertainties of the Monte Carlo simulations. This is true for other distributions as well. Hence, in all subsequent analysis the phase space distributions will be used. The figures of the previous section were all generated using this "decay mechanism".

data set	live time (hrs)	Mo films	position	bad detectors
E14R1–8	397	21	18–38	33
E16R1–24	1284	20	19–38	—
E16R25–28	197	20	19–38	21,24
E17R1–26	1595	36	3–38	1,2,11,21,32,40

Table 4.2: **Characteristics of the data sets** used in the analysis listed by experiment number and run numbers. The number of Mo films used is listed as well as the range of detectors above which they were placed.

4.3 Data Reduction

The data is divided into experiments and further subdivided into runs. A run is a 1–4 day period of continuous data taking collected on a single floppy disk. An experiment is a collection of runs which were made under similar circumstances. Table 4.2 lists the four data sets used in the analysis, by experiment and run numbers. Experiment 16 (E16) is broken into two parts (runs 1–24, runs 25–28) because of the loss of two detectors during a power failure. Experiment 16 differs from experiment 14 by the addition of formvar films (no ^{100}Mo) in the lower half of the detector array and the removal of a contaminated Mo film above detector 19. The formvar films were replaced by Mo films in experiment 17.

A number of Si detectors were not working properly during some of the data taking. These are listed as "bad detectors" in table 4.2. These detectors were either

data set	lower veto	individual vetoes
E14R1–8	≤ 19	32,34,40
E16R1–24	≤ 18	40
E16R25–28	≤ 25	40
E17R1–26	≤ 3	10,12,20,22,31,33,39

Table 4.3: **Detectors used as vetoes.** The "lower veto" vetoes on that detector and all others below it. The "individual vetoes" veto on only the detectors listed.

purposely disconnected because of low breakdown voltages or were not performing properly for most of the period in question. In the analysis it was decided only to keep events which were completely contained in the active volume of the array. For example in experiment 14 if an event deposited energy in detector 32 or 34 it would be vetoed because of the possibility of some unknown energy deposition in detector 33. Similarly, if detector 40 was part of an event, the event would be vetoed because of the possibility that some of the energy had escaped out of the top of the array. Table 4.3 lists the detectors used as vetoes in the various data sets. Events from the lower half of the array were not used if it did not contain any Mo, hence the use of a "lower veto" (see table 4.3) which eliminate any event depositing energy in this region. In experiment 14 the "lower veto" was set at detector 19 because of the contaminated film above detector 18.

Before vetoing events based on their position relative to bad detectors, a set of preliminary cuts was applied. A 120 keV discrimination level was used in the software on all detectors. If a Si detector had less than this amount of energy in it, the energy in the detector was set to zero and the total energy and size of the event was redefined. (This is the cut which enforces a zero in the first bin of figure 4.4). Secondly, one of the detectors in the event was required to have over 500 keV of energy. If not the event was vetoed. These cuts act as effective "software and hardware discriminators" (see section 3.7) eliminating channel to channel variations. Monte Carlo events were also subject to the same analysis. Table 4.4 shows the results. The geometric efficiencies listed there are based on an analysis of the Monte Carlo simulation using the preliminary cuts just described and the positioning of the Mo films relative to the veto detectors of table 4.3. The average geometric efficiency of .67 is obtained by dividing .053 total effective mole-years by .087 total mole-years.

The top curve on figure 4.6 shows the result of processing all data sets through the preliminary cuts and vetoes. The lower curve is obtained by an application of a set of secondary cuts after the above preliminary cuts. The secondary cuts, listed in order of decreasing importance; eliminate events with energy in only one detector; events which are discontiguous; events which have a non-zero "fast clock"; and events with energy in three or more detectors having less than 450 keV in a middle detector. The one detector events are dominated by alpha particles above an energy of 2 MeV. Discontiguous events are generated by multiple Compton scattering, beta-gamma and alpha-gamma decays. The "fast clock" records the

data set	mole-years	efficiency	effective mole-years
E14R1–8	.0076	.66	.0050
E16R1–24	.0234	.92	.0215
E16R25–28	.0036	.59	.0021
E17R1–26	.0524	.53	.0293
total	.087	.67	.058

Table 4.4: **Geometric efficiencies** based on Monte Carlo simulations given the relative placement of the Mo films and the"bad detectors". The effective mole-years is simply the product of the efficiency and the mole-years for that data set. The average geometric efficiency is listed for the "total" data set.

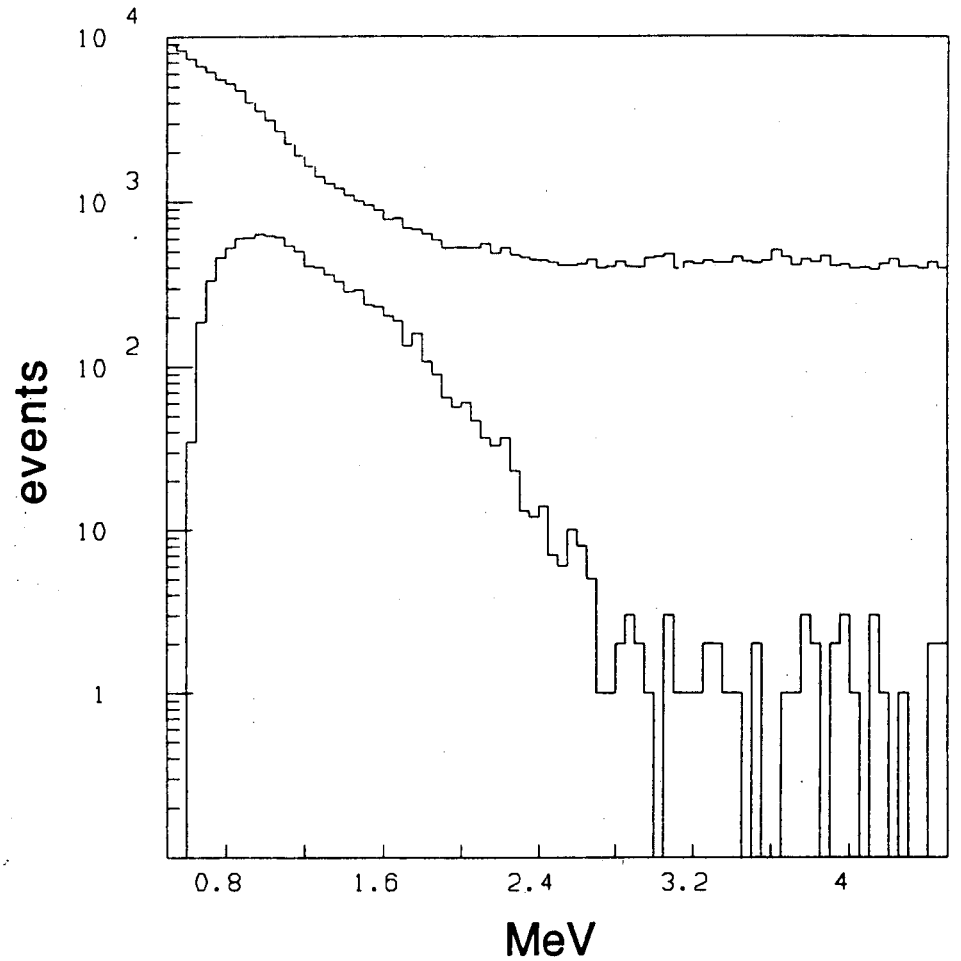

Figure 4.6: **Effect of the secondary cuts on the data.** The top curve show all events after preliminary cuts have been made. The lower curve shows the residual events after the application of the secondary set of cuts. Both sets of cuts are defined in the text.

presence of a second trigger pulse on the timing circuit during the readout of an event. The time from the beginning of the event to the second trigger is recorded (see section 3.5). These events are from ^{214}Bi and ^{212}Bi in the ^{238}U and ^{232}Th decay chains, respectively. Both of these are beta decays followed by alpha decays within the readout time of the beta decay event. If the alpha escapes the film with enough energy to trigger the timing circuit, the "fast clock" records the decay time and the event can be vetoed. The 450 keV cut on middle detectors is related to the minimum energy deposition required to traverse a Si detector and is discussed in detail on page 69. Most of the reduction seen in figure 4.6 is due to the elimination of events with energy in only one detector. In the energy interval from 2.7 to 3.0 MeV, the elimination of these events alone reduces the data by a factor of 76.

Given the sharp drop in the data rate above an energy of 2.7 MeV on the lower curve in figure 4.6, the search for neutrinoless double beta decay will be confined to the energy interval 2.7–3.0 MeV. Of the ten events in this region, seven of the them deposit energy in two detectors. The two-detector events are shown in the top histogram of figure 4.7. The events are plotted as a function of the ratio of the two energies. As was done before, the ratio is restricted to the interval 0.–1. by dividing by the larger energy. The candidate events seem to have more in common with the background events of the second histogram than with the Monte Carlo simulation of the bottom histogram. There are six candidate events below a ratio of .30. From the Monte Carlo simulation the probability of finding a two-detector event below a ratio of .30 is only 26%. Given one event above .30 and

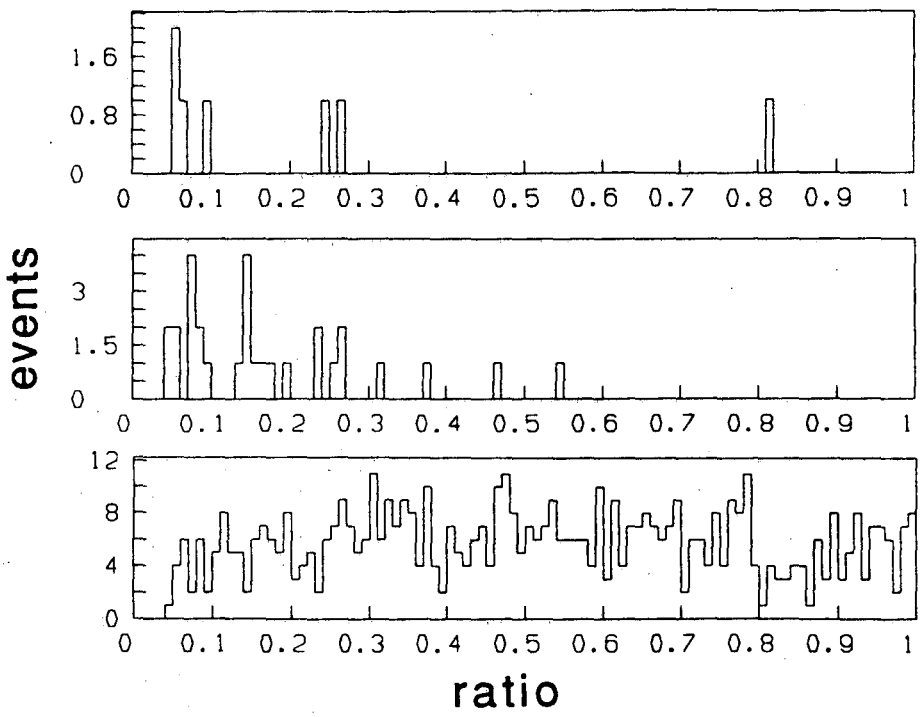

Figure 4.7: **Ratio of the energies for events with energy deposition in two detectors.** The top histogram shows the seven candidate events in the 2.7–3.0 MeV energy interval. The middle histogram shows background events from the interval 3.0–4.5 MeV. The bottom histogram shows the results of the Monte Carlo simulation.

six events below .30, the probability of this distribution being generated by double beta decay is .2%. Another way of comparing these histograms is by looking at the cumulative distribution function. This is the integral of the distribution plotted as a function of the ratio, with the total integral normalized to one. Figure 4.8 compares the seven two-detector candidate events to both the background sample and the Monte Carlo. It is clear that the candidates follow the background events much better than they do the Monte Carlo simulation. The conclusion is that these events are predominantly background and a cut in the ratio is introduced to eliminate all two-detector events with a ratio below .3. Figure 4.9 shows the effect of this cut on the data. The cut is applied uniformly to all two-detector events in the spectrum. The number of events above an energy of 2.7 MeV is reduced considerably.

There are four events remaining after the application of the ratio cut in the 2.7–3.0 MeV energy interval. Figure 4.10 show these events as a function of the number of detectors involved in the event. This should be compared with figure 4.2 of section 4.1, with the qualification that the number of one-detector events be reduced to zero and the number of two-detector events be reduced by 26%. The comparison shows there are far too many four-detector events. Given only one, two or three-detector event the expected number of four-detector events is $.11 \pm .11$. (This estimate includes the effect of the 2 detector ratio cut.) Excluding one-detector events and two-detector events below an energy ratio of .3, the Monte Carlo predicts the probabilities for two, three and four-detector events to be .47, .42 and .10 respectively. The probability of the distribution of figure 4.10 being

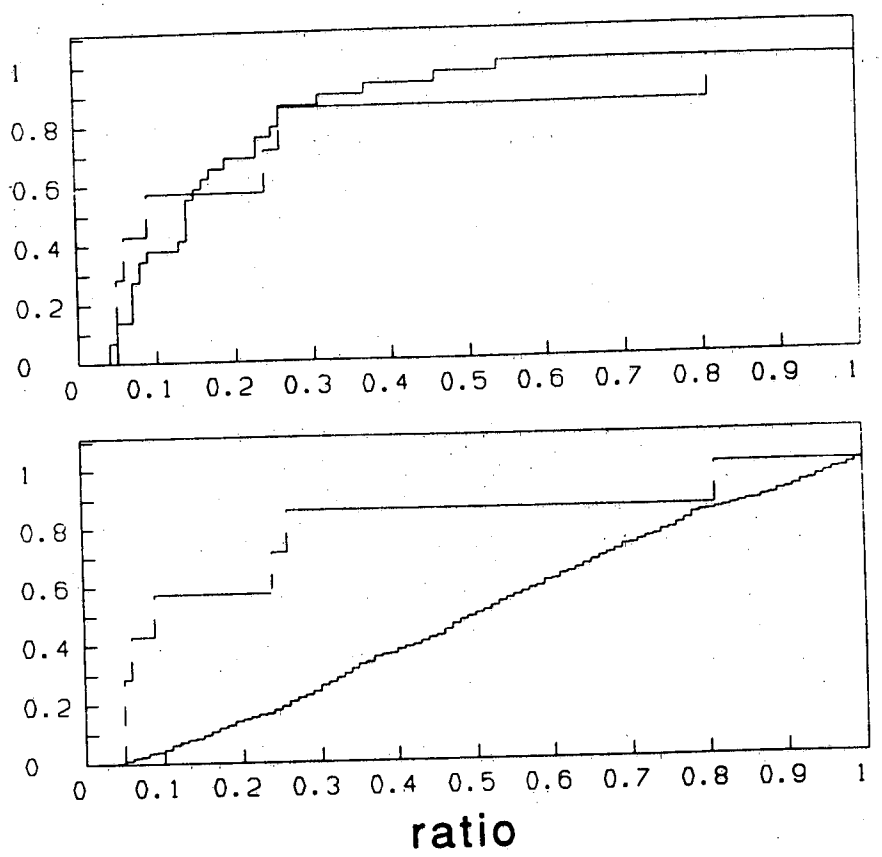

Figure 4.8: **Comparison of the cumulative distribution functions.** In both histograms the candidate events are represented by a dashed line. The solid line in the top histogram is the background sample of the previous figure. The solid line in the bottom histogram is from the Monte Carlo simulation.

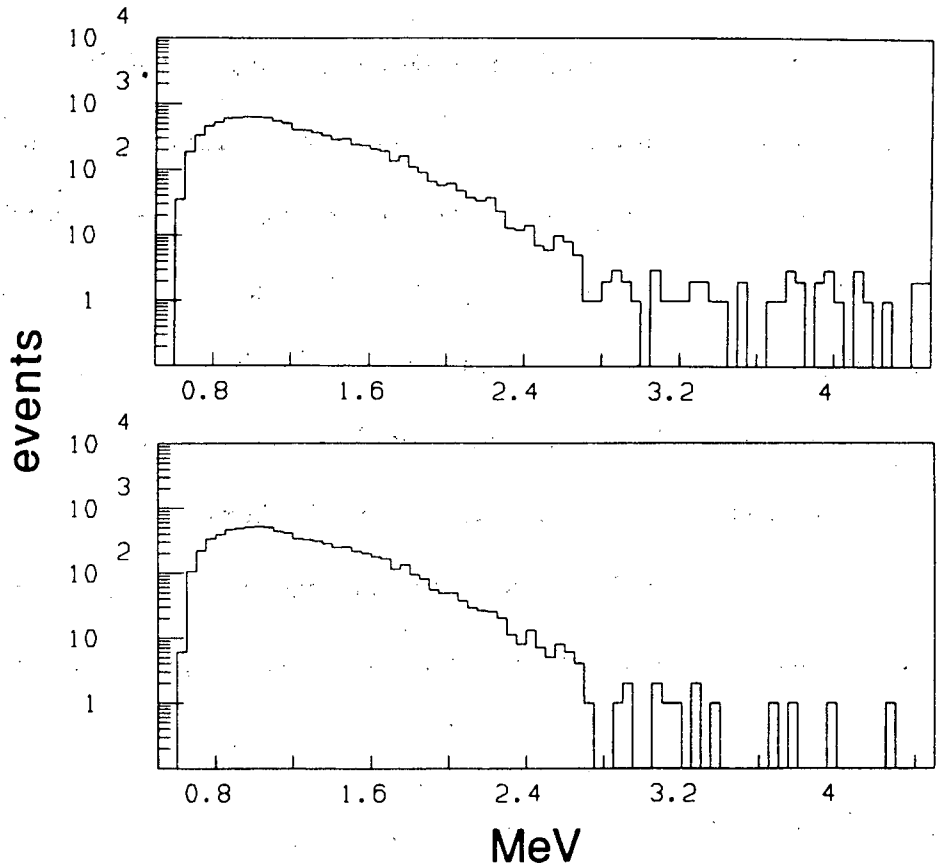

Figure 4.9: **Effect of the ratio cut on the data.** The top histogram shows the data before eliminating two detector events with an energy ratio of less than .3 (secondary cuts only). The bottom histogram shows the data after the cut on the ratio.

generated by double beta decay is then .2%. The four-detector events are therefore most likely background. These events are then eliminated from the data sample. Figure 4.11 shows the effect of this last and final cut on the data. In figure 4.12 the final result is shown on a linear scale for the interval 2.4–3.2 MeV.

Table 4.5 summarizes the results of the cuts on the efficiency and the data. The efficiencies are calculated by applying the same set of cuts to a Monte Carlo simulation of neutrinoless double beta decay. Excluding the selection of the 2.7–3.0 MeV energy interval, the cuts eliminate only 30% of the double beta decay events. Assuming the one remaining event is double beta decay and using the total cut efficiency of .40 found in table 4.5, the half-life for .058 effective mole-years of data is 1×10^{22} years. This one remaining event, a two-detector event from experiment 14 run 7, has a total energy of 2.911 MeV, with an energy ratio of .81.

4.4 Background Sources

The question arises as to the source of the events considered in the 2.7–3.0 MeV energy interval. Might the one remaining event be caused by double beta decay and if not what is the cause of this event and other nine events which survive the secondary cuts of the previous section?

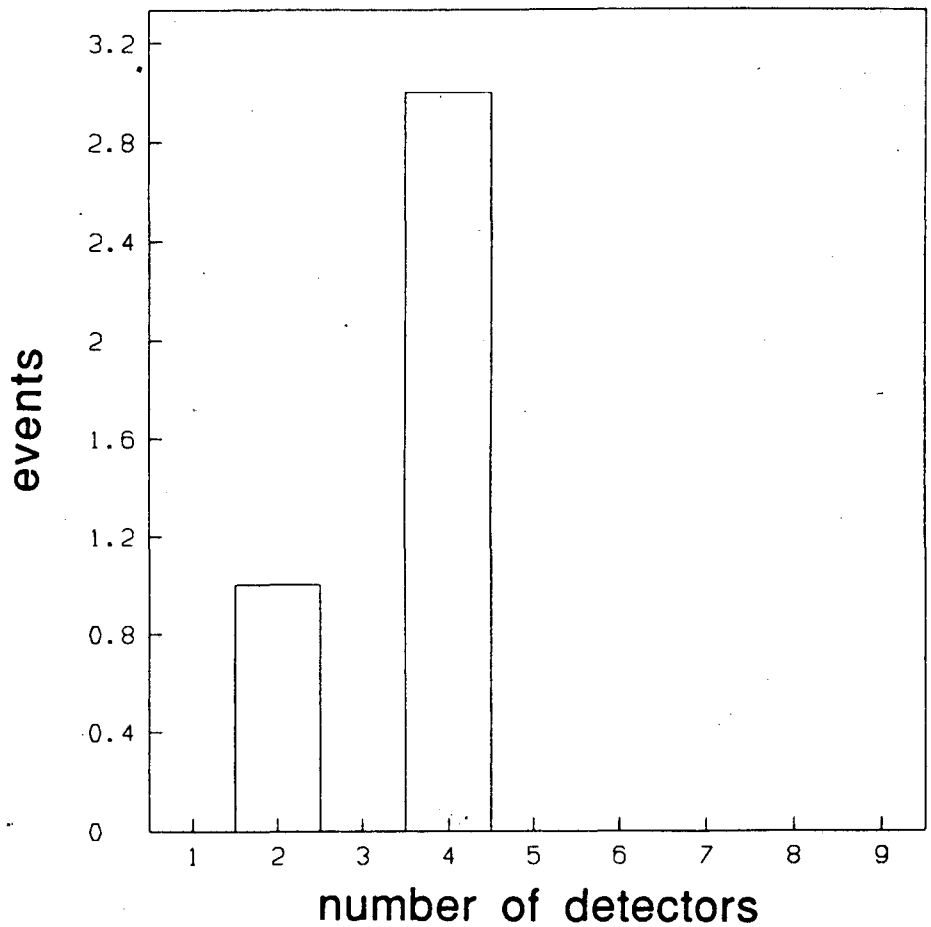

Figure 4.10: **Number of detectors involved in the remaining four candidate events.** This is the distribution after the application of the secondary cuts and the ratio cut.

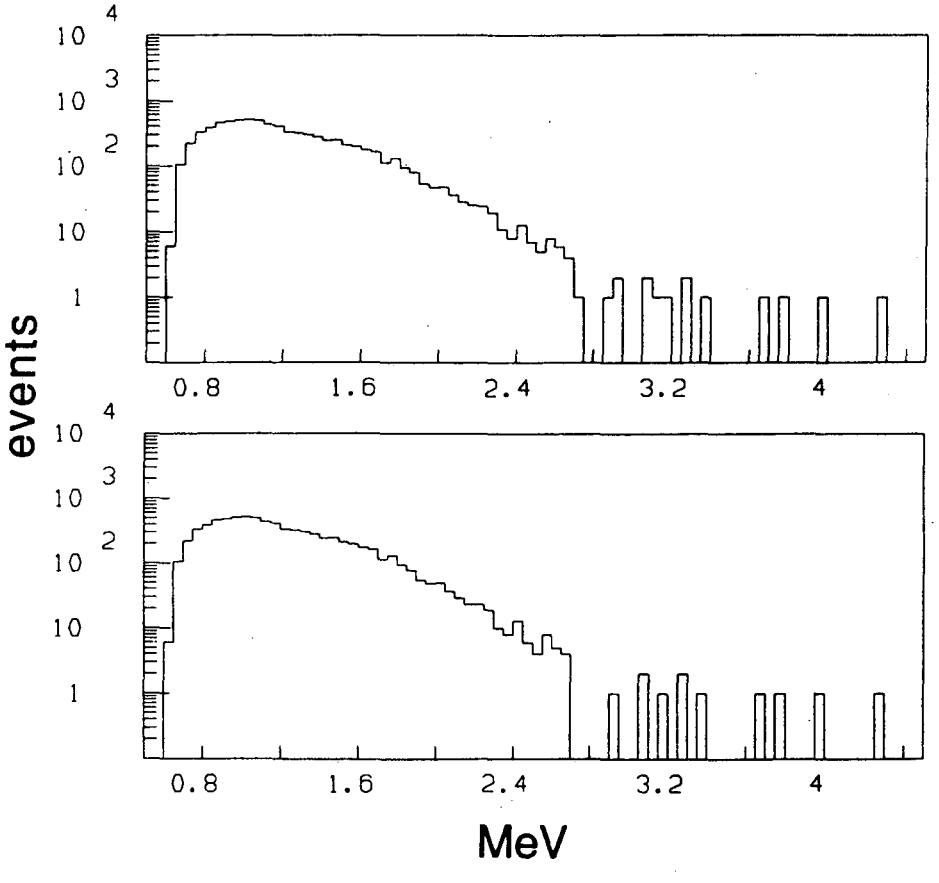

Figure 4.11: **Effect of the elimination of four-detector events on the data.** The top histogram shows the data after the secondary cuts and the ratio cut. In the bottom histogram the four-detector events have been eliminated.

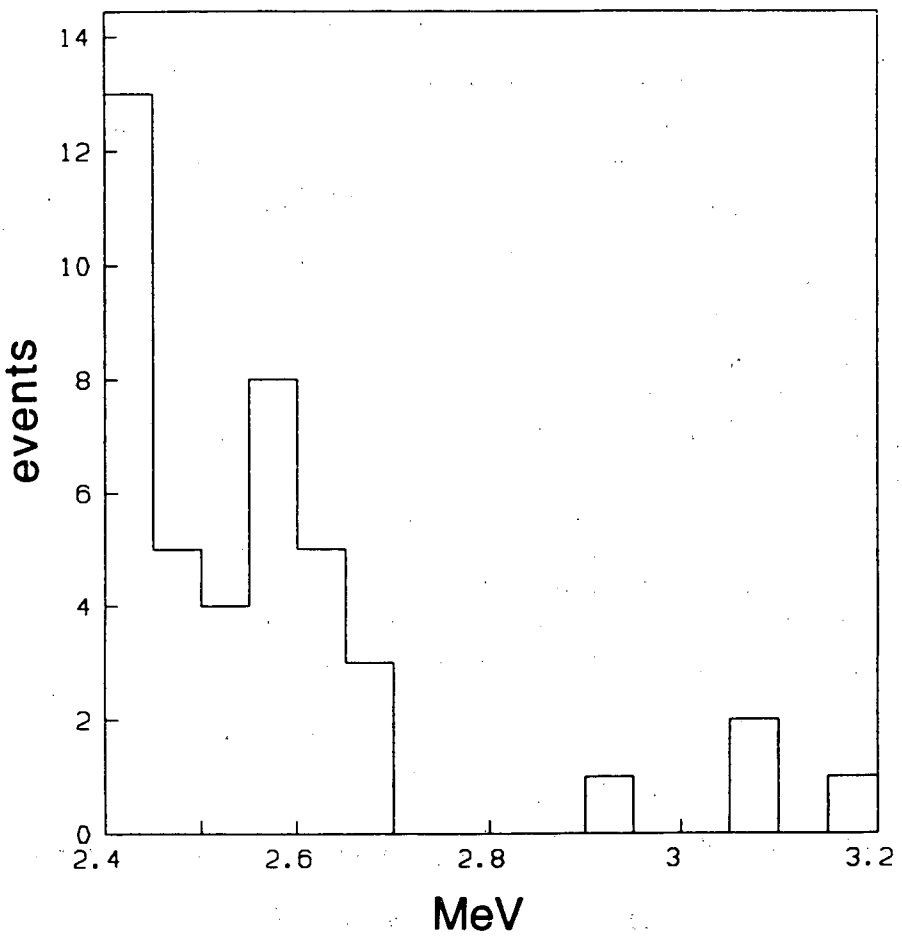

Figure 4.12: **Remaining events after the application of all cuts.**

data cuts	efficiency	events remaining
2.7 < total energy (MeV) < 3.0	.57	2517
Secondary cuts:		
one-detector events	.51	33
discontiguous events	.51	21
non-zero "fast clock" events	.51	11
events with < .45 MeV in middle detectors	.50	10
two-detector events with ratio < .3	.44	4
four-detector events	.40	1

Table 4.5: **Effect of various cuts on the data and efficiency in the interval from 2.7–3.0 MeV.** The cumulative effects of the elimination of each type of event is shown. Geometric efficiencies are not included in the above.

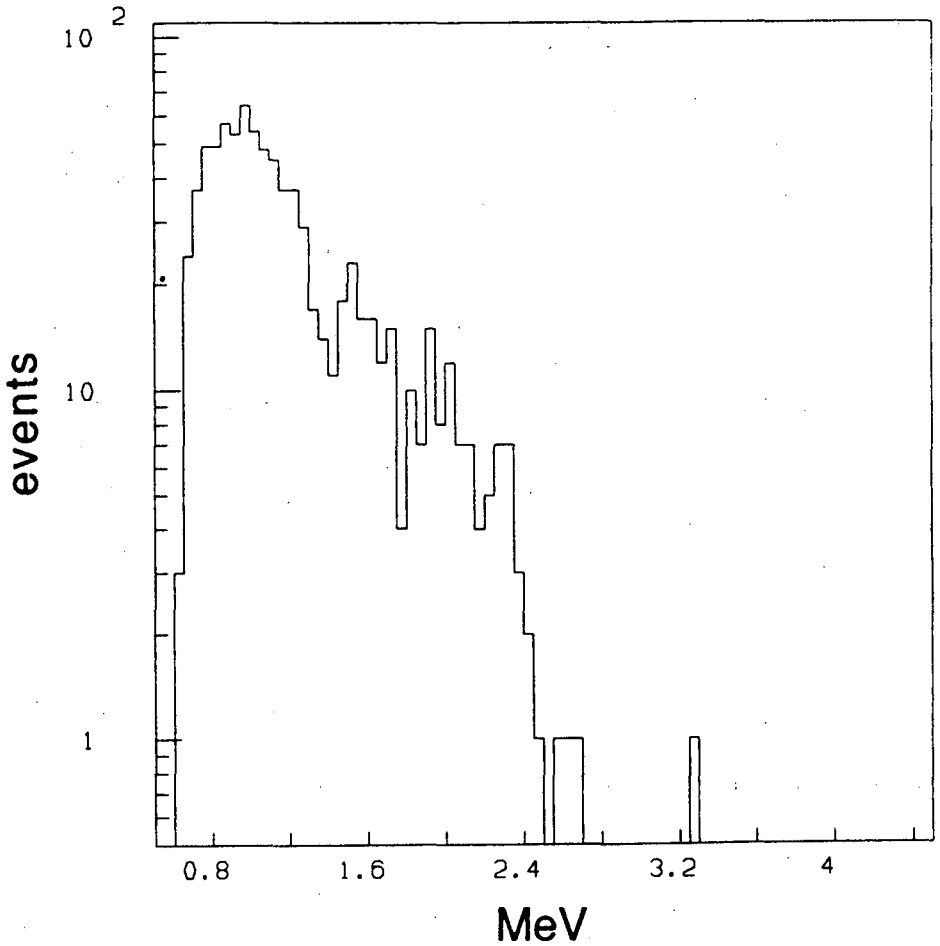

Figure 4.13: **Data collected on the formvar films after secondary cuts.**

4.4.1 Backgrounds from the Detector Array and Formvar Films

Figure 4.13 shows the data collected in experiment 16 on the blank formvar films (no ^{100}Mo) after the application of the preliminary and secondary cuts. The blank formvar films were produced in exactly the same manner as the Mo films, but without any ^{100}Mo . These films were placed above detectors 4–17. There is only one event above an energy of 2.7 MeV. This event deposits energy in two

detectors and has an energy ratio of .05. It would therefore be eliminated by application of the ratio cut. Of the four events above 2.5 MeV only one event at 2.65 MeV would survive application of the ratio cut. 1284 hours of data collection is shown in figure 4.13. The data in this figure need to be scaled up by a factor of 3.3 in order to make a proper comparison with the Mo data sample (bottom curve figure 4.6). Given the one event which survives the secondary cuts above an energy of 2.7 MeV, the expected number of events in the Mo data set is 3.3 ± 3.3. There are 46 events in the Mo data set above an energy 2.7 MeV which survive the secondary cuts.

The argument might be made that the above comparison is not valid because the blank films were placed in the lower half of the detector array and most of the data used in the search for neutrinoless double beta decay was collected from the upper half. In an earlier experiment however (E13), the entire array was empty. Without any films in the array, the data collection rate was lower by a factor of six. Approximately 1280 hours of data were collected in this mode. Because of problems with detectors in the lower half of the array most of the data were collected from the upper half. After the application of the secondary cuts there was only one event, a two-detector event with an energy ratio of .07, above an energy of 2.4 MeV. These data must be scaled up by a factor of 2.3 in order to make a proper comparison. The expected number of events is then 2.3 ± 2.3. This compares well with the estimate of 3.3 ± 3.3 from the formvar films. Given this result, it is safe to conclude that the dominant background source is in the ^{100}Mo sample itself.

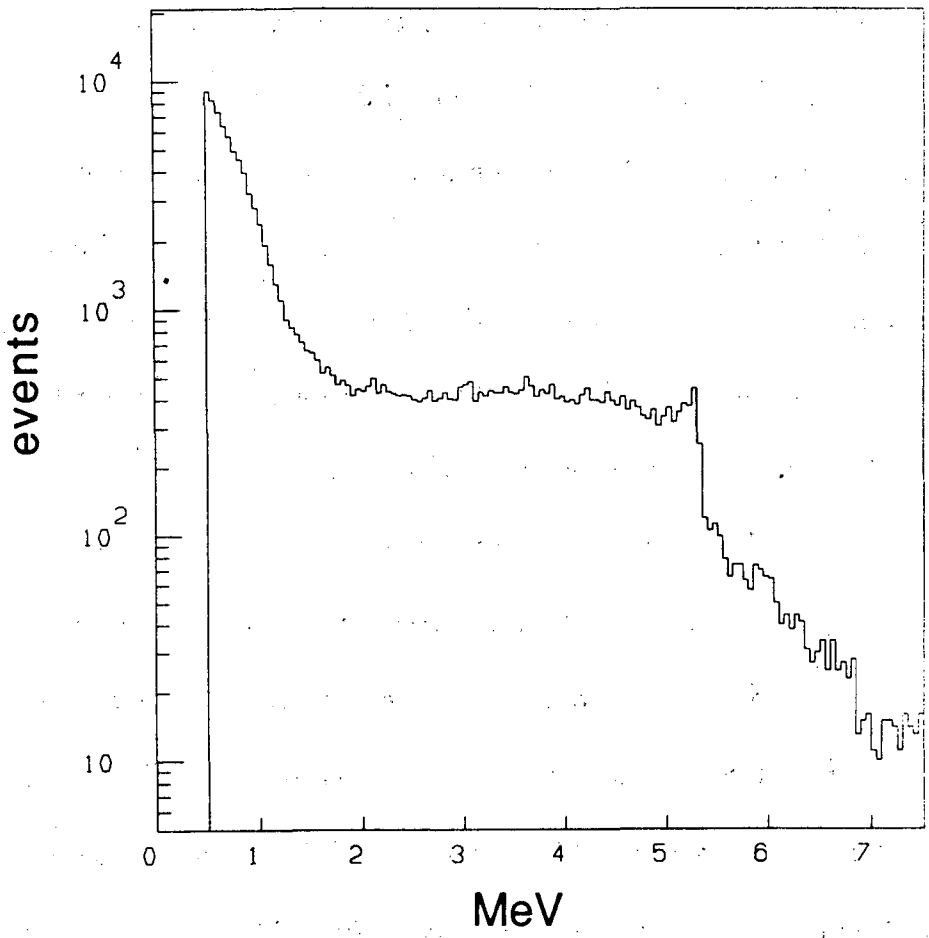

Figure 4.14: **One detector event spectrum from the Mo film data.**

4.4.2 Contamination in the ^{100}Mo

As mentioned above, the introduction of the Mo films into the Si detector array increased the data collection rate by a factor of six. The vast majority of these events deposit energy in only one detector. Figure 4.14 shows the one detector event spectrum for the Mo film data set. Above an energy of 2 MeV, it is very unlikely for a beta decay or a gamma ray conversion to deposit energy in only one detector. As a consequence these events are most likely alpha decays. In

particular the sharp rise in the spectrum below an energy of 5.3 MeV is from the alpha decay of ^{210}Po at the end of the ^{238}U decay chain. (The two major radioactive decay chains are shown in figure 4.15.) There is no evidence in figure 4.14 for an equivalent number of ^{238}U decays. There should be a comparable rise in the spectrum at 4.2 MeV and a number of similar jumps from other isotopes in the decay sequence, if the ^{210}Po and ^{238}U were in equilibrium. The ^{238}U decay chain need not be in equilibrium because of the long life-times of a number of isotopes in the chain. Chemical processing can selectively remove elements from the chain. It may then require as long as one million years before equilibrium is restored. Given the lack of evidence in the one-detector spectrum for other members of the ^{238}U decay chain, the most likely source of the ^{210}Po is the beta decay of ^{210}Pb with a 21 year half-life. If the ^{238}U chain were in equilibrium the ^{210}Po signal would imply a ^{238}U contamination in the ^{100}Mo of 33 ppb by weight, assuming a uniform distribution ^{238}U in the film.

Figure 4.14 also exhibits a small rise at 6.8 MeV. This may be due to ^{216}Po from the ^{232}Th decay sequence. The ^{232}Th chain has relatively few long lived isotopes. Other than ^{232}Th the longest lived isotopes are ^{228}Ra and ^{228}Th with half-lives of 5.7 and 1.9 years, respectively. All other isotopes have half-lives measured in days or less.

Because of the removal of one-detector events from the data sample, alpha decays by themselves cannot be a possible source of background contamination. Only beta decays with or without gamma ray emission in the Mo film are a potential problem. The large amount of ^{210}Pb associated with the ^{210}Po alpha decay

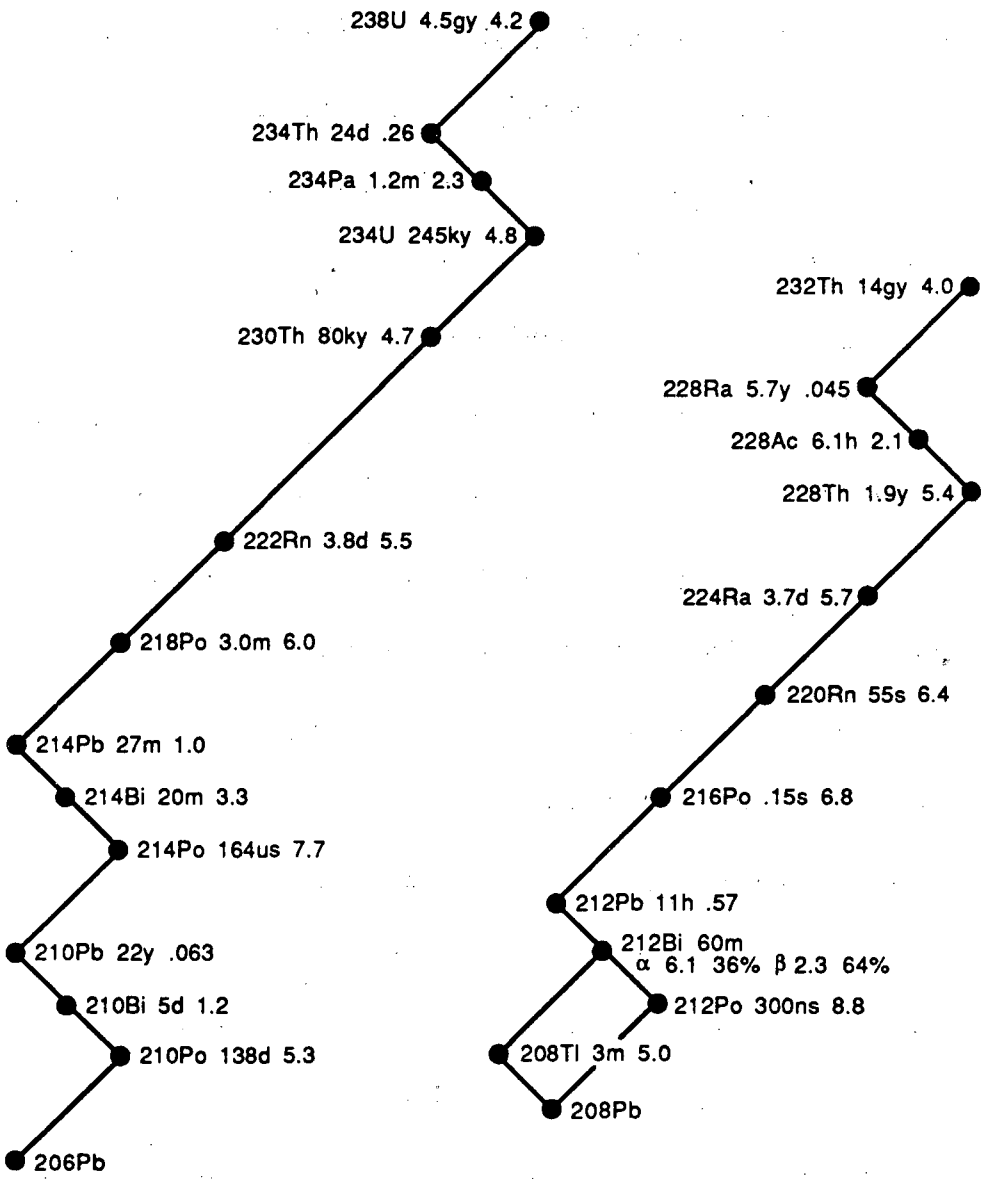

Figure 4.15: **The ^{238}U and ^{232}Th radioactive decay chains.** Each isotope is listed along with its half-life. The last number is the total decay energy (MeV) for beta decays and the most prominent alpha particle energy (MeV) for alpha decays.

need not be considered because in this region of the ^{238}U decay chain there are no beta decays above a decay energy of 1.2 MeV. There are only three decays in both the ^{232}Th and ^{238}U chains which can mimic neutrinoless double beta decay. They are the beta decays of ^{212}Bi and ^{208}Tl, and ^{214}Bi in the ^{232}Th and ^{238}U chains, respectively. The ^{212}Bi beta decay with a maximum energy release of 2.25 Mev, is followed by the 8.8 MeV alpha decay of ^{212}Po with a half-life of 300 nsec. The two events cannot be resolved by the electronics on the signal channel and may produce a multi-detector event with a energy release of up to 11 MeV. ^{208}Tl beta decays with an energy release of 5.0 MeV, but fortunately this occurs with the emission of a 2.6 MeV gamma ray over 99% of the time. If the gamma ray Compton scatters in the immediate vicinity of the decay or if it undergoes internal conversion ($< .02\%$), a background event in the 2.7–3.0 MeV energy interval could result. ^{214}Bi beta decays with an energy release of 3.3 MeV. This decay is to the ground state with no gamma ray emission 20% of the time. Consequently this decay is also a source of background. The ^{235}U decay sequence is not considered because there are no beta decays with an energy release above 1.5 MeV.

Figure 4.16 shows the distribution of decay times for events with a non-zero "fast clock" (see page 81) in the time interval from 0–2 μsec. From an exponential fit to this distribution above 250 nsec, a half-life of $284 + 54 - 39$ nsec is measured. This compares well with the actual ^{212}Po half-life of 300 nsec. As a consequence this data set constitutes a relatively clean sample of ^{212}Bi events. In this sample almost all of the events deposit energy in one or two detectors with only a very few events with energy in three detectors. In the energy interval from 2.7–3.0

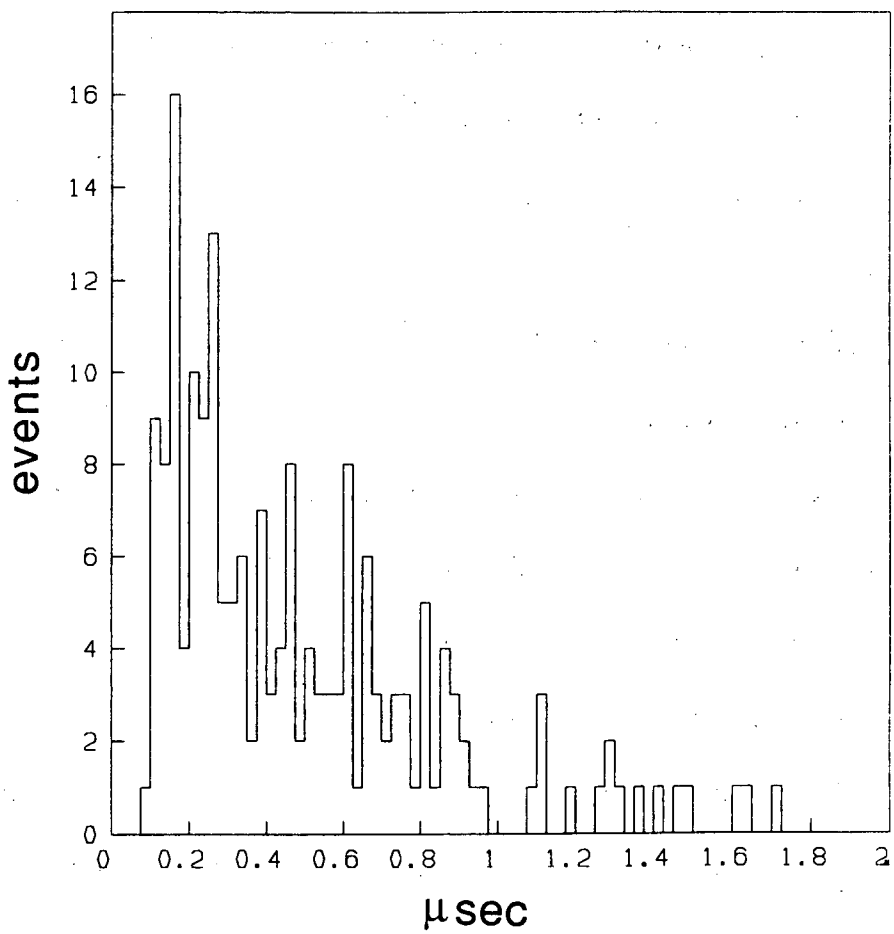

Figure 4.16: **Distribution of decay times in the interval from 0–2 μsec.** The distribution is obtained from all events with a non-zero "fast clock" in this range.

MeV there are only five events which pass the secondary cuts (apart from the requirement of a non-zero "fast clock"). These five events are all two-detector events. Figure 4.17 shows these events as a function of their energy ratio. It is clear that all but one of these events would be eliminated by a ratio cut of .3. A similar ratio distribution is obtained for the two-detector events in this sample above an energy of 3.0 MeV. A total of ten events would survive the ratio cut above 3.0 MeV.

In the energy interval from 2.7–3.0 MeV, the only difference between those ^{212}Bi events in the above sample and those without a "fast clock" tag is the time required for the ^{212}Po decay. It is clear from figure 4.16 that for decay times less than 100 nsec the fast clock is incapable of tagging the event. By using the half-life of 300 nsec and assuming that all events with a fast clock of less than 150 nsec are missed, it is estimated that 2.6 ± 1.2 events ^{212}Bi events pass the secondary cuts of the previous section in the energy interval from 2.7–3.0 MeV (There are 7 such two-detector events in the Mo data sample). Of these only an estimated $.5 \pm .5$ events pass all cuts. Above 3.0 MeV the estimated number of ^{212}Bi events which pass all cuts is 7.7 ± 2. This accounts for almost all of the 10 events above 3.0 MeV in the Mo data set.

The beta decay of ^{214}Bi is also followed by a Po alpha decay. The half-life for this decay is 164 μsec. Because of the longer half-life, the beta decay energy can be resolved. By choosing events with a "fast clock" in the time interval from 2-2000 μsec a sample of these events is obtained. From an exponential fit to the time distribution a half-life of 147 ± 13 μsec is measured, consistent with the actual 164

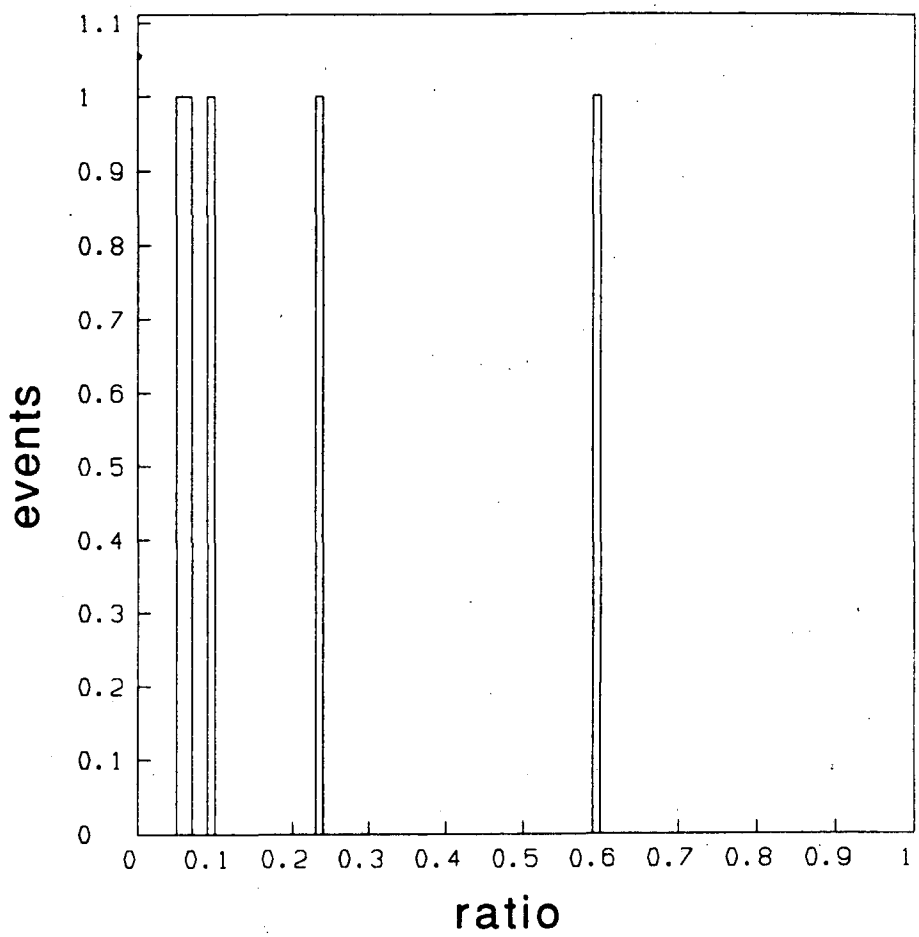

Figure 4.17: **Ratio of the energies for ^{212}Bi events** in the energy interval from 2.7–3.0 MeV. All of these events which pass the secondary cuts are two detector events.

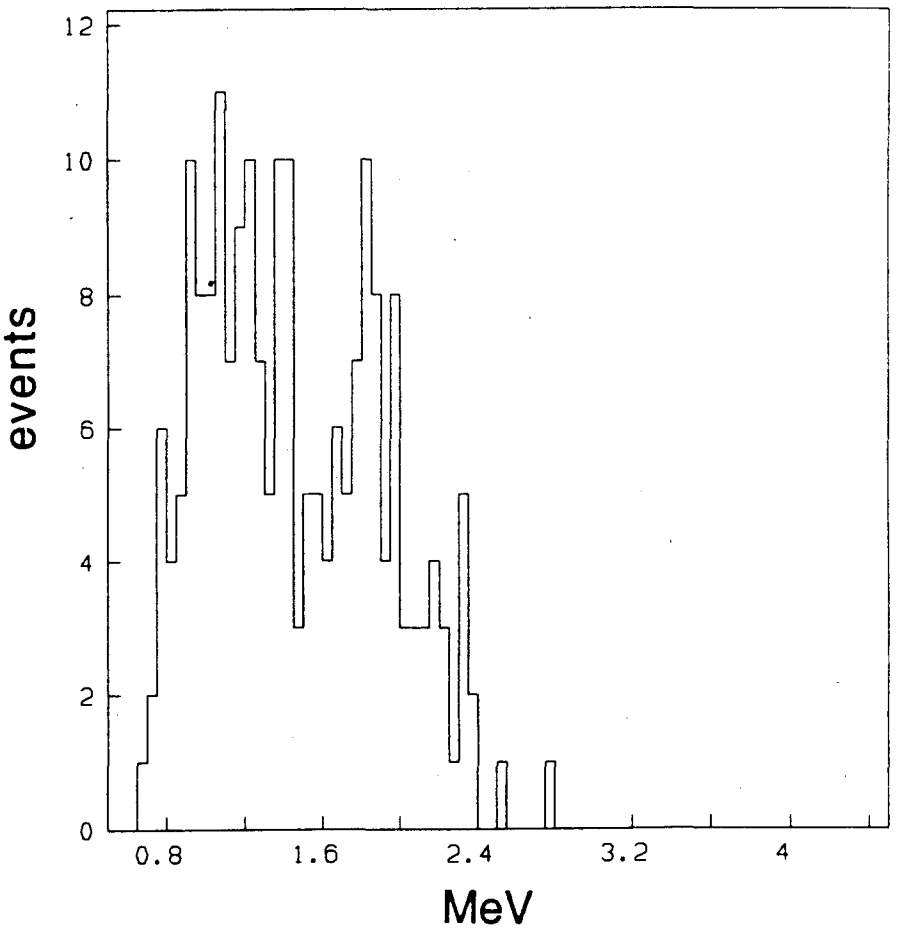

Figure 4.18: **^{214}Bi spectrum after all cuts.** The sample is obtained by requiring the "fast clock" to be the 2-2000 μsec range.

μsec half-life. Figure 4.18 shows the energy spectrum obtained after the application of all cuts (excluding the requirement of a zero in the "fast clock"). Unlike ^{212}Bi the beta decay alone can generate a background event. Events untagged by a "fast clock" are produced because the alpha particle may not escape the Mo film. From reference [32] the estimated range of a 7.7 MeV alpha particle is 15.4 mg/cm^2. Assuming a uniform distribution of ^{214}Bi in the film, the probability that the alpha escapes the film with enough energy to set the "fast clock" is .22. As a

consequence it is expected that, after all cuts, the one event above 2.7 MeV in figure 4.18 corresponds to 4.5 ± 4.5 events in the Mo data set. A better estimate of this number can be obtained by using the two events above 2.4 MeV and the relative probability, calculated using the Monte Carlo, that a ^{214}Bi beta decay event above 2.4 MeV is actually above 2.7 MeV of .23. The result is 2.1 ± 1.5 events after all cuts.

The number of background events expected after all cuts from both Bi decays is 2.6 ± 1.6. From this alone it is clear that the one remaining event is most likely background. Not considered so far is the ^{208}Tl decay. The problem with estimating the contribution from this decay is that there is no Monte Carlo program currently available to accurately calculate gamma ray conversions in our geometry and determine the relative number of these events which would pass the cuts of section 4.3. A simple estimate of the Compton scattering probability of the 2.6 MeV gamma ray within two detectors of the beta decay, indicates contribution of the ^{208}Tl decay might be six times that of ^{212}Bi. It is not clear what effect the cuts would have on these events. Most of the gamma ray conversion probability comes from those gamma rays traveling perpendicular to the axis of symmetry of the detector array. As a consequence it might be expected that many of these events deposit energy in only one detector and would be eliminated. Similarly it is difficult to estimate the number of three-detector events which would be removed by requiring the middle detector in the event to contain a minimum energy of 450 keV. The event might also still be discontiguous because of multiple Compton scattering in the stack or the emission of a second gamma ray. If it is assumed

	^{212}Bi	^{214}Bi	^{208}Tl	total
events	.5±.5	2.1±1.5	3±3 ?	> 2.6

Table 4.6: **Estimated number of events after all cuts** from the three problem beta decay in the naturally occurring decay chains. The ^{208}Tl estimate is much more incertain than the statistical error shown, hence it is not included in the total which is listed as a lower limit as a consequence.

that the application of all cuts has the same effect on ^{208}Tl as ^{212}Bi, there would be 3±3 ^{208}Tl events after all cuts. The estimate of 2.6 events after all cuts should then be taken as a lower limit on the contribution of both the ^{238}U and ^{232}Th decay chains to the backgrounds. Table 4.6 summarizes the results of this section.

From the ^{212}Bi and ^{214}Bi background samples above, the total ^{232}Th and ^{238}U contamination for the ^{100}Mo can be measured. Assuming these chains are both in equilibrium, the contamination is $6 \pm .4$ and $3.4 \pm .2$ ppb by weight, respectively. This is in good agreement with the Oak Ridge neutron activation measurements of section 3.2, which measure the ^{238}U and ^{232}Th directly and do not require this assumption. Consequently, except for the ^{210}Pb contamination (33 ppb ^{238}U equivalent), these results are consistent with the equilibrium of both decay chains.

4.5 Half-life Limit

The standard formula used to set a limit on the half-life assuming no signal events are present in the data is,

$$\tau_{1/2} \geq \frac{\epsilon \ln(2) N_a t}{\sqrt{n_b}}$$

where ϵ is the efficiency; N_a the number of atoms of source material; t is the live time; and n_b is the number of events in the region of interest (assumed to be background). It is clear from the previous section that the one remaining event, after all cuts, is most likely background. As a consequence the half-life limit is 1×10^{22} years. This is the same as the half-life calculated assuming the one remaining event is double beta decay, only because there is a single event.

The square root is used in the above formula because it is the standard deviation in the number of background counts and as such is a measure of the number of real double beta decay events that may be hidden in the sample. This limit is usually referred to as the 68% confidence limit. This comes from integrating a one sided gaussian probability distribution with a most probable value of zero from zero to one standard deviation. (The interval from zero to plus infinity is normalized to one. Values less than zero are not included because they correspond to negative decay rates.) If values below zero are included the confidence level is 84%.

In our case, with only one event, gaussian statistics do not apply. Poisson statistics must be used. The standard deviation is still the square root of the number of events. As in the gaussian case, the confidence level is obtained by

integrating the probability distribution from the most probable value to the most probable value plus one standard deviation, if it is assumed that values of the rate lower than the most probable values are not allowed. Given one event, the most probable value and the standard deviation are both equal to one. From reference [33] the confidence level is 45%. If the values below the most probable are included in the integration, this becomes 59%.

Because of the ambiguity associated with assigning a confidence level to the limit calculated by use of the above formula, this value is referred to as a 1σ limit. This terminology has become common in the double beta decay literature in recent years and it is adopted here.

Chapter 5

Conclusion

The ^{100}Mo neutrinoless double beta decay half-life limit set by this experiment of 1×10^{22} years, a factor of five larger than the best previous ^{100}Mo result [28], places restrictions on various double beta decay parameters, such as the effective Majorana neutrino mass and right-handed current couplings for light neutrinos and the effective inverse mass for heavy neutrinos.

Using equation (2.29) and scaling the results of Engel et.al. [20] at the end of section 2.5, this experiment sets an upper limit on the effective Majorana neutrino mass, $\langle m_\nu \rangle$, of 14 eV. This should be compared to the limits set by the best ^{76}Ge and ^{82}Se experiments (see table 2.4). Again using the calculation of Engel et.al. [20], the ^{76}Ge and ^{82}Se limits are 7.3 eV and 32 eV, respectively. Given the variability of matrix elements listed in table 2.1, the ^{76}Ge, ^{82}Se and presumably the ^{100}Mo mass limits may be as much as factor of seven lower.

Since none of the ^{100}Mo matrix elements necessary to extract the right-handed current couplings have been calculated, the constants C_4 and C_5 in equation (2.33)

are calculated using the ^{76}Ge matrix elements of reference [21] in equation 2.17 of reference [34] along with the ^{100}Mo kinematical factors of table 3.4 in reference [8]. The ^{100}Mo kinematical factors of reference [8] are first renormalized to conform to the conventions of references [21] and [34]. Assuming both the effective mass, $\langle m_\nu \rangle$, and the effective right-handed coupling, $\langle \lambda \rangle$, are zero in equation (2.33), $\langle \eta \rangle$ is less than 6×10^{-8}. Similarly, if $\langle m_\nu \rangle$ and $\langle \eta \rangle$ are assumed to be zero then $\langle \lambda \rangle$ is less than 5×10^{-6}. The best upper limits on these quantities come from the UCSB/LBL ^{76}Ge experiment. They are calculated in reference [21] to be 3.6×10^{-6} for $\langle \lambda \rangle$ and 2.8×10^{-8} for $\langle \eta \rangle$.

For heavy neutrinos the best limit on the effective inverse mass, again coming from the UCSB/LBL ^{76}Ge experiment, is 8×10^{-8}/GeV [25]. If one assumes there is only one heavy neutrino involved, this number implies that the probability of finding an electron neutrino in a 1 GeV mass eigenstate is less than 8×10^{-8}. For a 100 GeV mass eigenstate, the probability is less than 8×10^{-6}. Scaling the ^{76}Ge result by using the appropriate kinematical factors in equation (2.31) and the ^{100}Mo half-life limit (this again assumes ^{100}Mo and ^{76}Ge matrix elements are equal), leads to a ^{100}Mo limit on the inverse mass of less than 20×10^{-8}/GeV.

The above discussion clearly shows this experiment to be within a factor of 2–3 of the best double beta decay results to date on all quantities of physical interest. This is quite remarkable considering only .053 effective mole-years of data has been collected. The UCSB/LBL ^{76}Ge experiment, which has produced the best results, has collected 9 mole-years. Table 5.1 summarizes the limits set by this experiment and for comparison purposes also lists the UCSB/LBL results.

	$\tau_{1/2}$ (years)	$\langle m_\nu \rangle$ (eV)	$\langle \lambda \rangle$	$\langle \eta \rangle$	$\langle \frac{1}{m_\nu} \rangle$ $(\text{GeV})^{-1}$
^{100}Mo	1×10^{22}	14	5×10^{-6}	6×10^{-8}	20×10^{-8}
^{76}Ge	5×10^{23}	7.3	3.6×10^{-6}	2.8×10^{-8}	8×10^{-8}

Table 5.1: **Limits set by this experiment and the UCSB/LBL Ge experiment.** The half-lives quoted are lower limits. All other quantities are upper limits. The assumptions made in the calculation of the ^{100}Mo limits are described in the text.

Bibliography

[1] R. Davis et.al., Phys. Rev. Lett. **20**, 1205 (1968)

[2] S.P. Mikheyev and A.Yu. Smirnov, Sov. J. Nucl. Phys. **42**(6), 913 (1985)

L. Wolfenstein, Phys. Rev. **D17**, 2369 (1978)

[3] K. Hirata et.al., Phys. Rev. Lett. **58**, 1490 (1987)

T. Haines, in Telemark IV: Neutrino Masses and Neutrino Astrophysics, Ashland, Wisconsin, 1987, ed. by V. Barger, F. Halzen, M. Marshak and K. Olive (World Scientific, Singapore, 1987) p. 63

[4] T. Kirsten et.al., in Proceedings of the International Symposium on Nuclear Beta Decay and Neutrinos, Osaka, Japan 1986, ed. by T. Kotani, H. Ejiri and E. Takasugi (World Scientific, Singapore, 1986) p. 81

[5] O. K. Manuel, in Proceedings of the International Symposium on Nuclear Beta Decay and Neutrinos, Osaka, Japan 1986, ed. by T. Kotani, H. Ejiri and E. Takasugi (World Scientific, Singapore, 1986) p. 71

[6] S. R. Elliot, A. A. Hahn, and M. K. Moe, Phys. Rev. Lett. **59**, 2020 (1987)

[7] W. C. Haxton and G. J. Stephensen, Jr., Prog. in Part. and Nucl. Phys. **12**, 409 (1984)

[8] A comprehensive review of the experimental and theoretical aspects of double beta decay can be found in M. Doi, T. Kotani and E. Takasugi, Prog. of Theor. Phys. Supp., **83**, (1985)

[9] S. P. Rosen, Proc. Moriond Workshop on Massive Neutrinos, ed. by J. Tran Thanh Van (Hup Lee Printing Co., Pte Ltd., Singapore, 1984) p. 53
S. P. Rosen, Phys. Rev. **D29**, 2535 (1984)

[10] T. Yanagida, Proc. Workshop on Unified Theory and Baryon Number in the Universe, ed. by Sawada and Sugamoto, KEK (1979)
M. Gell-Mann, P. Ramond and R. Slansky, Supergravity, ed. by van Niewenhuizen and Freedman (North-Holland, Amsterdam, 1979)

[11] B. Kayser, Phys. Rev. **D30**, 1023 (1984)

[12] M. Doi et.al., Prog. Theor. Phys. **70**, 1331 (1983)

[13] J. Shecter and J. W. F. Valle, Phys. Rev. **D25**, 2951 (1982)
L. Wolfenstein, Phys. Rev. **D26**, 2507 (1982)

[14] M. N. Georgi, S. L. Glashow and S. Nussinov, Nucl. Phys. **B193**, 297 (1981)

[15] F. T. Avignone III et.al., Proceedings of the Annual Meeting of the Division of Particles and Fields of the American Physical Society, Salt Lake City, Utah, 1987, ed. by C. DeTar and J. Ball (World Scientific, Singapore, 1987) p. 359

F. T. Avignone III, in Telemark IV: Neutrino Masses and Neutrino Astrophysics, Ashland, Wisconsin, 1987, ed. by V. Barger, F. Halzen, M. Marshak and K. Olive (World Scientific, Singapore, 1987) p. 248

[16] D. O. Caldwell et.al., Phys. Rev. Lett. **59**, 419 (1987)

[17] B. Kayser, Proceedings of the Annual Meeting of the Division of Particles and Fields of the American Physical Society, Eugene, Oregon, August 12-15, 1985, ed. by R. Hwa (World Scientific, Singapore, 1986) p. 397

[18] B. Kayser and A. S. Goldhaber, Phys. Rev. **D28**, 2341 (1983)

[19] S. P. Rosen, in Proceedings of the 1981 International Conference of Neutrino Physics and Astrophysics, Maui, Hawaii, ed. by R. J. Cence, E. Ma and A. Roberts (High Energy Physics Group, Dept. Of Physics and Astronomy, University of Hawaii, Honolulu, Hawaii) Vol. 2, p. 76

[20] J. Engel, P. Vogel and M. R. Zirnbauer, submitted to Phys. Rev. C
P. Vogel (private communication)

[21] T. Tomoda and A. Faessler, Phys. Lett. B **199**, 475 (1987)

[22] K. Grotz, H.V. Klapdor, Nucl. Phys. A **460**, 395 (1986)

[23] O. Civitarese, A. Faessler and T. Tomoda, Phys. Lett. B **194**, 11 (1987)

[24] R. G. Winter, Phys. Rev. **99**, 88 (1955)

[25] D. O. Caldwell in Proceedings of the XXIII International Conference on High

Energy Physics, Berkeley, Ca., 1986, ed. by S. C. Loken (World Scientific, Singapore, 1987) Vol.2, p. 951

[26] N. Kamikubota and T. Watanabe, in Telemark IV: Neutrino Masses and Neutrino Astrophysics, Ashland, Wisconsin, 1987, ed. by V. Barger, F. Halzen, M. Marshak and K. Olive (World Scientific, Singapore, 1987) p. 281

[27] A. A. Hahn, in Telemark IV: Neutrino Masses and Neutrino Astrophysics, Ashland, Wisconsin, 1987, ed. by V. Barger, F. Halzen, M. Marshak and K. Olive (World Scientific, Singapore, 1987) p. 312

[28] Yu. G. Zdesenko, in Proceedings of the International Conference Neutrino'82, Balatonfüred, Hungary, 1982, ed. by A. Frenkel and L. Jenik (Budapest, 1982) p. 209

[29] C. Liquori, in Telemark IV: Neutrino Masses and Neutrino Astrophysics, Ashland, Wisconsin, 1987, ed. by V. Barger, F. Halzen, M. Marshak and K. Olive (World Scientific, Singapore, 1987) p. 307

[30] A review of semiconductor detector fabrication and use titled "The Solid State Ionization Chamber" can be found in G.T. Ewan, Nucl. Inst. and Meth. **162**, 75 (1979)

[31] L. Landau, Journal of Physics **8**, 201 (1944)

[32] L. Northcliffe and R. Schilling , Nucl. Data Tables A**7**, 233 (1970)

[33] Particle Data Group, Phys. Lett. B**170**, 53 (1986)

[34] T. Tomoda et.al., Nucl. Phys. A **452**, 591 (1986)

LAWRENCE BERKELEY LABORATORY
TECHNICAL INFORMATION DEPARTMENT
UNIVERSITY OF CALIFORNIA
BERKELEY, CALIFORNIA 94720